# A Conserved Landscape of Chemokine Receptor Co-expression Defines the Functional States of CD8+ T Cells in Melanoma

**Authors:** Rodney Macedo[1,2]*, David. W. Harle[1,2], Kevin Hoffer-Hawlik[3], Ximi K. Wang[1,2], Thomas McMahon-Skates[1], Alexandra Matschiner[1], Kirubel Belay[1], Yvonne M. Saenger[4], Ben Izar[1,2,5], Elham Azizi[2,3,4], Ran Reshef[1,2,5]*

**Affiliations:**

[1]Columbia Center for Translational Immunology, Department of Medicine, Columbia University Irving Medical Center, New York, NY 10032, USA.

[2]Herbert Irving Comprehensive Cancer Center, Columbia University Irving Medical Center, New York, NY 10032, USA

[3]Department of Biomedical Engineering, Columbia University, New York, NY, USA. Irving Institute for Cancer Dynamics, Columbia University, New York, NY 10027, USA.

[4]Department of Oncology, Albert Einstein College of Medicine, Bronx, NY 10461, USA.

[5]Department of Medicine, Division of Hematology & Oncology, Columbia University Irving Medical Center, New York, NY, USA.

*To whom correspondence should be addressed: ran.reshef@columbia.edu, rmacedo@igtp.cat

**One Sentence Summary:** Co-expression of CCR5, CXCR6, and CXCR3 provides a functional 'code' that separates T-cell-mediated anti-tumor efficacy from off-target toxicity, enabling the selection of superior cells for safer and more effective cancer immunotherapies.

## Graphical Abstract

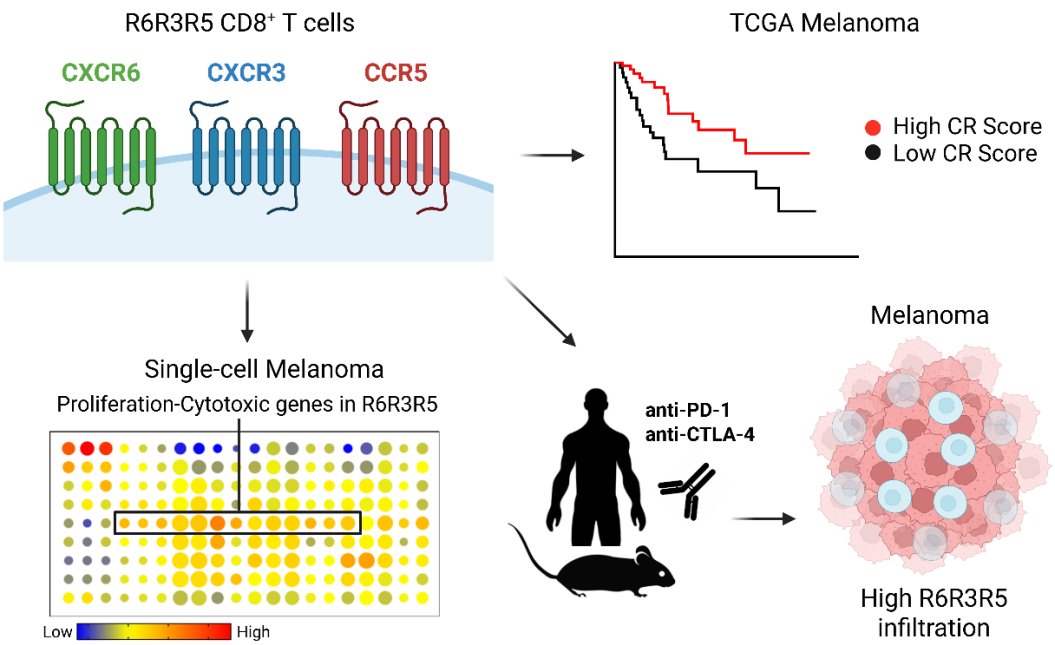


## Highlights

- CXCR6, CXCR3 and CCR5 co-expression signature stratifies patient survival in human melanoma
- $CD8^+$ T cells co-expressing CXCR6, CXCR3 and CCR5 are critical effectors with high proliferative, cytotoxic, and activation profile in human and mice melanoma
- $CD8^+$ T cells co-expressing CXCR6, CXCR3 and CCR5 drive anti-tumoral responses during checkpoint blockade in both human and mice

**Abstract**:

Cancer immunotherapies, from checkpoint blockade to adoptive cell therapies like tumor-infiltrating lymphocytes (TILs), have revolutionized cancer treatment but are limited by variable efficacy and significant toxicities. A central challenge is identifying ideal T-cell populations that effectively eliminate tumors without causing off-target damage, a distinction not captured by existing biomarkers. We show that co-expression patterns of chemokine receptors (CRs) CXCR3, CCR5, and CXCR6 on $CD8^+$ T cells provide a functional "code" defining subsets with divergent roles in on-target immunity versus off-target inflammation. In mouse and human melanoma, a triple-positive ($CXCR3^+CCR5^+CXCR6^+$) T-cell subset is essential for tumor control, and its genetic signature correlates with positive clinical response, while a distinct $CCR5^+CXCR6^+$ subset drives liver immune-related adverse events (IRAEs). Crucially, this CR code reveals that immunotherapy actively reshapes T-cell trafficking patterns, uncovering profound heterogeneity within conventional populations and distinguishing potent anti-tumor progenitors from cells predisposed to exhaustion or off-target migration. This work establishes CR co-expression as a practical tool, providing a surface marker-based strategy to identify and enrich optimized T cells for adoptive therapies, thereby offering a framework to uncouple efficacy from toxicity.

**Article**:

Combined PD-1 and CTLA-4 blockade (P1C4) leads to impressive and durable clinical responses in melanoma [1], and many other cancers [2,3]. Though transformative, only a subset of patients responds, and immune-related adverse events (IRAEs) account for the high incidence of grade 3-4 adverse events, treatment-related mortality and high discontinuation rates, limiting broader application of combination therapies [4-11]. Both tumor rejection and IRAEs induced by checkpoint inhibitors are fundamentally governed by lymphocyte migration into tumors and healthy tissues [12-14]. The recent approval of autologous tumor-infiltrating lymphocytes (TILs) in metastatic melanoma and the fact that the majority of patients do not achieve long-term benefit from this approach [15-17] further underscore the need for deeper understanding of T-cell populations with an ideal profile that combines effective trafficking to the tumor, potent effector function, high proliferative capacity (stemness), ability to resist suppressive signals, and low exhaustion state, resulting in an effective anti-tumor response.

Chemokines are proteins that control the trafficking of T cells and other leukocytes into different tissues by interacting with chemokine receptors (CR) expressed on the cell surface [18]. Previous studies have investigated the role of CRs individually. Elevated expression of certain chemokine receptors such as CXCR3 and CCR5 or their ligands is associated with increased intratumoral T-cell infiltration and favorable outcomes in melanoma [19-21] and other cancers [22-27]. These studies led to the experimental use of CR inhibitors in cancer patients with mixed results [28-31], possibly due to failure to account for the biologic reality that leukocytes co-express multiple CRs which collectively orchestrate their migration and potentially other functions [32]. This highlights a significant gap in our understanding and an unmet need in identifying T-cell populations with an ideal profile - combining potent tumor trafficking and effector function while avoiding healthy tissues. This may facilitate the development of novel pharmacologic or adoptive cell therapy approaches in cancer.

Here, we address this challenge by investigating the co-expression patterns of key inflammatory CRs. We provide evidence in both mice and humans that the coordinated expression of CXCR3, CCR5, and CXCR6 defines distinct $CD8^+$ T-cell subsets with divergent roles in mediating tumor clearance and immune-related toxicity following dual checkpoint blockade. Our findings may help design future therapies that modulate leukocyte migration to improve the efficacy and reduce immune-related toxicity of cancer immunotherapies.

## A T-cell Chemokine Receptor Signature Stratifies Patient Survival in Melanoma

To identify CRs central to the anti-tumor T-cell response and conserved across multiple cancers, we conducted an *in-silico* analysis of 11,323 tumor transcriptomes from 33 human cancers in the Cancer Genome Atlas (TCGA). This screen revealed that the inflammatory CR genes *CXCR3*, *CCR5*, and *CXCR6* show both high expression and variance (Extended Data 1a). This receptor triad formed a distinct signature that correlated strongly with T-cell specific genes in comparison with other leukocyte populations (Fig. 1a top and Supplementary Table 1). The same was true when analyzing 475 human samples from TCGA melanoma (Fig. 1a bottom and Extended Data 1b). Consistent with this, the primary ligands for CXCR3, CCR5 and CXCR6 correlated with T-cell- and macrophage-specific genes, but not with tumor cells, B cells or fibroblasts (Extended Data 1c).

While the expression level of each receptor individually was higher in "brisk" tumors [33] (characterized by dense lymphocytic infiltrate) versus "non-brisk" PANCAN and melanoma tumors, the combinatorial CR score proved superior. Specifically, CR scores (based on *CXCR6*, *CXCR3* and *CCR5* expression) were not only associated with significant differences between these tumor types (Fig. 1b, Extended Data 1d) but were also linked to improved overall survival uniquely within brisk tumors (Fig. 1c). Similarly, CR scores were associated with higher abundance of $CD8^+$ T cells [34] and IFN-γ [35] in tumors, identifying a survival benefit even within $CD8^+$ and IFN-γ dominant tumors (Fig. 1b, Extended Data 1e-g). This was reinforced by an analysis of transcriptional data from metastatic [36] and primary [37] human melanoma where CR scores were higher in non-recurrent (Extended Data 1h) or responder (Extended Data 1i) tumors. Interestingly, differentially expressed genes (DEGs) from samples with higher co-expression of *CXCR6*, *CXCR3*, and *CCR5* are related to T cell activation pathways (Extended Data 1j and 1k). Taken together, these data establish that *CXCR3*, *CCR5*, and *CXCR6* form a core inflammatory T-cell gene signature, and their distinct co-expression correlates with better survival across tumor types.

**Combinatorial Chemokine Receptor Expression Reveals a Hierarchy of T-cell Effector Programs**

To determine if different CR co-expression patterns define distinct functional states, we performed *in-silico* single-cell analysis of treated and untreated human metastatic melanoma tumors [38]. As shown in Extended Data 2a, after identifying eight major cell populations using cell type-specific genes, we focused on $CD8^+$ T cells ($CD8^+$), classifying them into nine unique subsets based on the combinatorial expression of *CXCR6*, *CXCR3* and *CCR5* (using *CCR7* to demarcate the naive subset within the triple negative cells) (Fig. 1d left). This approach revealed extensive CR heterogeneity in the TME (Fig. 1d right) and established that multi-receptor patterns, rather than single markers, were required to delineate functionally distinct cell states.

Transcriptional profiling of CR-defined subsets uncovered a functional continuum across $CD8^+$ T cells, establishing a hierarchy from naive to terminally differentiated states (Fig. 1e and 1f, Extended Data 2b and 2c, and Supplementary Table 2). At one end of the spectrum, the triple-negative (3N+) and CXCR3-only (R3) subsets were the least differentiated, expressing markers of stemness and a naive state. These cells also expressed chemokines that attract dendritic cells and showed signs of early activation and regulation, suggesting a progenitor-like role with early cytotoxic potential. In contrast, the co-expression of CCR5 and/or CXCR6 marked cells with potent effector programs. Dual- and triple-expressing subsets were enriched for cytotoxic molecules, cytokines, and chemokines. The **triple-positive (R6R3R5) subset** emerged as a critical effector phenotype, showing the highest expression of genes related to proliferation, cytotoxicity, and activation. Other dual-expressing subsets represented distinct intermediate states; for example, R3R5 TILs were highly proliferative, while R6R3 TILs displayed a resident-effector profile with high expression of cytotoxic molecules but lower proliferation. Finally, CXCR3-negative TILs appeared more terminally differentiated, characterized by high expression of exhaustion markers. Within this group, subsets displayed unique profiles: R5 cells resembled an immature memory state, while R6R5 and R6 subsets were more akin to short-lived effector cells, with R6R5 being more cytotoxic and R6 showing more tissue residency markers. These findings corroborate that specific

combinations of CXCR3, CCR5, and CXCR6 expressions define a detailed functional map of $CD8^+$ T cell diversity within the tumor microenvironment.

**Chemokine Receptor Expression Marks a Differentiation and Activation Trajectory in TILs**

To map the evolution of CR expression during T cell maturation, we analyzed a second human metastatic melanoma single-cell RNA-seq dataset [39]. We used pseudotime inference, a computational approach which orders cells along a continuous phenotypic trajectory, in this case from naive (*TCF7*-expressing) to terminally differentiated (*TOX*-expressing) $CD8^+$ T cells [40]. To better study the increase/decrease of CR expression and its variability across pseudotime, we performed a rank sort (Extended Data 2d), and then we used a sliding window (300 cells) to smooth the CR expression for the four genes across the inferred pseudotime (Extended Data 2e). The analysis revealed a distinct and sequential pattern of CR expression along this differentiation trajectory (Fig. 1g). The trajectory begins with naive cells expressing high levels of *CCR7*, which is progressively lost as they mature (Fig. 1h). *CXCR3* expression emerges early and is sustained throughout most of the cell's journey, whereas *CCR5* appears and increases to peak expression in intermediate states. Finally, *CXCR6* expression is acquired late in the trajectory, marking the most differentiated cells and correlating with *TOX* expression. Taken together, these results suggest that as T-cells mature within the tumor, they undergo programmed, sequential co-expression of *CXCR3*, *CCR5* and *CXCR6* and subsequently a gradual loss of these receptors at the terminally differentiated phase. This evolution underscores that combinatorial dynamic expression patterns, rather than static expression of a single receptor, are critical for accurately characterizing the functional state of TIL subsets and their distinct roles in mediating anti-tumor efficacy.

**A Conserved Chemokine Receptor Code Defines Functional T-cell Programs in Mice and Humans**

To confirm if the CR-defined subsets identified in tumors represent a fundamental aspect of T-cell biology, we analyzed their protein expression in healthy human and mouse lymphocytes using multiparametric flow cytometry (Fig. 1a, Extended Data 3 and Supplementary Table 3). This analysis revealed that the CR co-expression "code" is a conserved feature that defines a functional hierarchy (Fig. 2b-c, Extended Data 4a-c). In both species, the least differentiated, naive-like subsets (3N+ and R3) were the most abundant and largely corresponded to traditional Naive ($T_N$) and Central Memory ($T_{CM}$) populations. In contrast, the Effector Memory ($T_{EM}$) population was highly heterogeneous, comprising the full spectrum of CR-defined subsets (Fig. 2d-e, Extended Data 4d-f).

Crucially, our CR framework uncovered profound functional divergence even within the classically defined TEM population (Fig. 2f and Extended Data 4g). For example, R3 $T_{EM}$ cells retained stem-like properties (high TCF1/7), while subsets co-expressing multiple CRs, like R6R3R5, were primed for cytotoxicity and proliferation. Other subsets showed exhausted phenotypes (high PD-1, LAG3) or possessed distinct tissue-homing potentials, expressing receptors that support either tumor infiltration (CCR2) or mucosal sites (CCR6, CCR9). Altogether, these results confirm at the protein level that CR co-expression defines conserved, functionally distinct T-cell subsets. This framework uncovers critical heterogeneity within the traditional $T_{EM}$

population, distinguishing cells with potent anti-tumor potential (R6R3R5) from those predisposed to exhaustion or migration to other tissues.

**Distinct T-cell CR Subsets Drive On-Target Efficacy Versus Off-Target Inflammation During Checkpoint Blockade**

To dissect the *in vivo* roles of CR-defined subsets in the context of immunotherapy, we studied their response to dual PD-1 and CTLA-4 blockade (P1C4) in a B16-F10 melanoma model (Fig. 3a). This combination was chosen as it was most effective at increasing $CD8^+$ $T_{EM}$ cells compared to single-agent therapy (Extended Data 5a) and is clinically relevant due to its high efficacy in human melanoma. Following treatment, we observed increased $CD8^+$ T and $T_{EM}$ cell percentages in both tumor and liver (Fig. 3b). While liver enzymes remained unchanged in this model, immunohistochemistry revealed a significant increase in $CD3^+$ T cells in the liver, indicating subclinical inflammation (Extended Data 5c-e). These results established a robust model to simultaneously investigate the mechanisms of tumor control and the tissue-specific drivers of immune-related toxicity.

P1C4 therapy profoundly and selectively altered the distribution of CR-defined subsets in peripheral tissues (Figure 3c). In the tumor, treatment drove a dramatic expansion of the triple-positive R6R3R5 subset, while causing a contraction of single-expressing R3 and R5 cells. Conversely, in the liver, P1C4 selectively increased the R6R5 subset. These changes were not observed in the spleen or tumor-draining lymph nodes (TdLNs), highlighting a tissue-specific effect (Extended Data 5f). This divergence suggests that distinct CR programs mediate on-target anti-tumor activity versus off-target immune infiltration, a hypothesis supported by a corresponding increase in the ligands for CXCR3, CCR5 (e.g., CXCL9, CXCL10, CCL5) in both tumor and liver supernatants after treatment, whereas CXCR6 ligand (CXCL16) is higher only in the tumor (Extended Data 5g).

Genetic knockout models proved that this co-expression is essential for the therapeutic effect. In the context of P1C4, mice lacking either *CCR5* or *CXCR6* lost the ability to increase their intratumoral $CD8^+$ $T_{EM}$ cells, losing any significant change in CR-defined subsets, an effect not seen in untreated knockout mice (Fig. 3d-e), demonstrating the role is specific to the immunotherapy context. Furthermore, the P1C4-mediated increase in the tumor's favorable CD8/Treg ratio was modestly reduced in *CCR5* knockout mice and completely eliminated in *CXCR6* knockout mice (Fig. 3f). These data demonstrate that the full anti-tumor response to P1C4 requires the functional contribution of T cells co-expressing all three receptors.

A competitive short-term homing assay further clarified these roles (Fig. 3g). As expected, CXCR3 was confirmed to be critical for T-cell trafficking into the tumor, TdLNs, and liver specifically under P1C4 treatment (Fig. 3h and Extended Data 5h-i). The roles of the other receptors were more complex; for instance, CXCR6-deficient cells accumulated in lymphoid tissues after P1C4 treatment, suggesting impaired migration to the tumor or inability to establish tissue residency status. Altogether, these experiments establish that while CXCR3 acts as a key director of T-cell trafficking, the functional outcome of P1C4 therapy—driving either potent tumor rejection or

immune-mediated toxicity—is dictated by the specific co-expression patterns of CXCR3, CCR5, and CXCR6 on responding T cells.

## Anti-Tumor T-cell Subsets Defined by CR Co-expression Expand with Checkpoint Blockade and Correlate with Clinical Response

To validate our findings in a clinical context, we first analyzed PBMC samples from melanoma patients, comparing dual Immune Checkpoint Blockade (ICB)-treated and ICB-naive patients (Supplementary Table 4). ICB-treated patients had significantly higher percentages of $CD8^+$ T cells in their blood compared to ICB-naive patients (Extended Data 6a-b). Strikingly, dual ICB treatment led to a significant increase in the circulating triple positive R6R3R5 subset (Fig 4a), which our preclinical data identified as having potent effector function. This expansion of triple positive cells in human blood mirrors our findings in splenic $CD8^+$ from mice treated with P1C4 (Extended Data 6c). The overall profile of CR-defined subsets is modified by ICB (Fig. 4b and Supplementary Fig. 4a), which also altered their immunophenotype (Fig 4c). Similar to what we found in normal donors, 3N+ and R3 have higher naive/stemness markers such as TCF1/7, R6R3R5, R3R5, R6R5 and R5 have a greater cytotoxicity signature and increased expression of KLRG1, and those exhausted are mainly R6R3, R6R5, R6 and R6R3R5 expressing high amounts of PD-1, LAG-3, and TIM-3.

Interestingly, certain CR-defined subsets in ICB-treated patients have an altered profile compared to ICB-naïve patients: 3N+ and R3 subsets have a significant decrease in AhR while R6 subsets show a significant increase in KLRG1. Moreover, R5, R3R5, R6R3R5 and R6R5 subsets show a significant decline of PD-1 expression, suggesting receptor occupancy by therapeutic antibody [41]. These results confirm in humans that P1C4 treatment increases the proportion of CR-defined subsets responsible for tumor control but also modifies the functional properties of these subsets.

To determine if CR-defined subsets within the human TME are associated with clinical outcomes, we analyzed the single-cell transcriptional dataset from metastatic melanoma patients treated with ICB [39]. This analysis revealed that *CXCR6* expression is significantly higher (Mann-Whitney test; $P$=0.0095) in responder patients than non-responders, whereas *CCR7*, *CXCR3* and *CCR5* show no association with response (Extended Data 6d). More importantly, the gene signatures for the CXCR6-co-expressing subsets - R6R3R5, R6R3 and R6R5- are all significantly enriched in tumors of responder patients (Mann-Whitney test; $P$<0.05) (Fig. 4d). These results confirm in humans that ICB reshapes the landscape of circulating T cells to favor the expansion of the highly functional R6R3R5 subset. Critically, they also establish that the enrichment of CXCR6-co-expressing T-cell subsets within the tumor itself is a key feature of a successful anti-tumor response to immunotherapy.

## Discussion

A central challenge in cancer immunotherapy—from checkpoint blockade to adoptive cell therapies like TILs—is uncoupling potent anti-tumor efficacy from treatment-limiting, off-target toxicity. This requires a deeper understanding of the T-cell subsets that mediate these opposing outcomes. While the roles of individual chemokine receptors in T-cell trafficking are well-studied,

248 the combinatorial "code" they form to dictate specific functional states has remained unclear.
249 Our study addresses this gap, demonstrating that the co-expression of CXCR3, CCR5, and CXCR6
250 provides a conserved functional map of $CD8^+$ T cells in both mice and humans, allowing for the
251 prospective identification of T-cell subsets responsible for on-target efficacy versus off-target
252 inflammation.

253 Our analysis reveals that this CR code defines a fundamental and conserved T-cell developmental
254 trajectory. In healthy individuals, we found that the hierarchy progresses from naive-like,
255 progenitor cells expressing primarily CXCR3 (R3 subset) to highly differentiated effector cells co-
256 expressing all three receptors (R6R3R5 subset). Crucially, this framework uncovers profound
257 functional heterogeneity within traditionally defined populations like effector memory T cells
258 ($T_{EM}$). Within the $T_{EM}$ pool, our code distinguishes stem-like progenitors (R3) from highly cytotoxic
259 and proliferative effectors (R6R3R5) and exhausted subsets, a level of functional resolution not
260 achievable with conventional markers. Importantly, our analysis demonstrates that specific
261 combinations of these three receptors, rather than single markers, are required to accurately
262 define the functional state and potential of a T cell.

263 In the context of cancer immunotherapy, this framework provides a powerful lens to dissect the
264 mechanisms of both tumor response and IRAEs. Our preclinical data show that dual ICB
265 selectively expands the triple-positive R6R3R5 subset in the tumor, a population essential for
266 therapeutic efficacy. Conversely, the therapy promoted the accumulation of a distinct
267 $CCR5^+CXCR6^+$ (R6R5) subset in the liver, a common site of IRAEs. This finding mechanistically links
268 a specific, identifiable T-cell subset to off-target toxicity, providing a cellular target for future
269 strategies aimed at mitigating IRAEs. The fact that genetic deletion of either CCR5 or CXCR6
270 abrogated the therapeutic effect of ICB underscores that the coordinated function of all three
271 receptors on the R6R3R5 subset is non-redundant and essential for a successful anti-tumor
272 response.

273 Ultimately, our findings set up this CR code not just as a prognostic biomarker but as a practical
274 tool for developing better immunotherapies. The prognostic value of single chemokine receptors
275 has been inconsistent across studies, likely because, as we show, the functional output of T cells
276 is associated with receptor combinations. The true translational potential of our work lies in its
277 direct application to cell-based therapies. The surface markers of this code are readily detectable
278 by high-dimensional flow cytometry, offering a straightforward strategy to identify and
279 prospectively isolate the most desirable T-cell populations. For adoptive cell therapies, such as
280 TILs, this framework provides a clear rationale for enriching the final product with the highly
281 proliferative and cytotoxic R6R3R5 subset while potentially depleting populations like R6R5 that
282 may contribute to toxicity. This approach offers a tangible path forward to engineer more potent
283 and safer immunotherapies, improving the therapeutic window by maximizing anti-tumor
284 activity while minimizing collateral damage.

285 While the expression profile of CRs and other trafficking molecules in immune cells has been
286 previously described in healthy humans [42,43] and in cancer [44,45], the functional impact of their co-
287 expression on the anti-tumor response requires multiparametric, single-cell analysis. Using

genetic datasets and high-dimensional flow cytometry, our study simultaneously analyzed multiple CRs with functional markers and transcription factors to clarify the critical role of CR co-expression in shaping anti-tumor T-cell responses.

## Data and code availability

All data generated in this study are included in this published article and its supplementary information. Code relating to data processing and figure generation is available in our GitHub repository. Patient information is available on the supplementary table 4. Any additional information required to reanalyze the data reported in this paper is available from the corresponding authors upon request.

## Acknowledgements

We thank the CCTI Biobank and Flow Cytometry Cores. We gratefully acknowledge the Columbia Institutional Review Board and all patients who generously consented to participate in this study, as well as the Institutional Animal Care and Use Committee. We are also grateful to Megan Sykes, Siu-Hong Ho, Audrey Baeyens, and Claudia Gutierrez-Chavez for helpful discussions.

## Funding

E.A. is supported by NIH NCI R00CA230195, NHGRI R01HG012875, and grant number 2022-253560 from the Chan Zuckerberg Initiative DAF, an advised fund of Silicon Valley Community Foundation. E.A. and R.R. are supported by a Columbia University HICCC programmatic pilot award. R.R. is supported by NIH R01-HL143424, P30-CA013696, and CA171008(DOD) grants. J.L.M. is supported by NIH NHGRI R35HG011941 and NSF CBET 2146007. The CCTI/HICCC Flow Cytometry Core is supported by NIH grants S10OD020056 and S10OD030282.

## Author contributions

R.M., D.H., and R.R., conceived the study. R.M., D.H., K.H.H., X.W., A.M., and K.B. performed sample processing and data collection. R.M., D.H., K.H.H., X.W., T.M.S., K.B., Y.S., B.I., E.A., and R.R. provided clinical samples and data and maintained regulatory oversight. R.M., D.H., K.H.H., X.W., and T.M.S., analyzed the data. R.M., D.H., K.H.H., X.W., T.M.S., A.M., K.B., Y.S., B.I., E.A., and R.R. interpreted the data. R.M., R.R., E.A. and K.H.H. wrote the manuscript.

## Declaration of interests

R.R. reports consulting or advisory role with Allogene, Bayer, Gilead Sciences, Incyte, TScan, Orca Bio, Pierre Fabre Pharmaceuticals, CareDx, Sana Biotechnology, Sail Biomedicines and Autolus, and research funding from Atara Biotherapeutics, Incyte, Sanofi, Immatics, Abbvie, Takeda, Gilead Sciences, CareDx, TScan, Cabaletta, Synthekine, BMS, J&J, Allogene, Genentech, Vittoria Therapeutics, AstraZeneca, Kinomica and Imugene.

**Figure 1.**

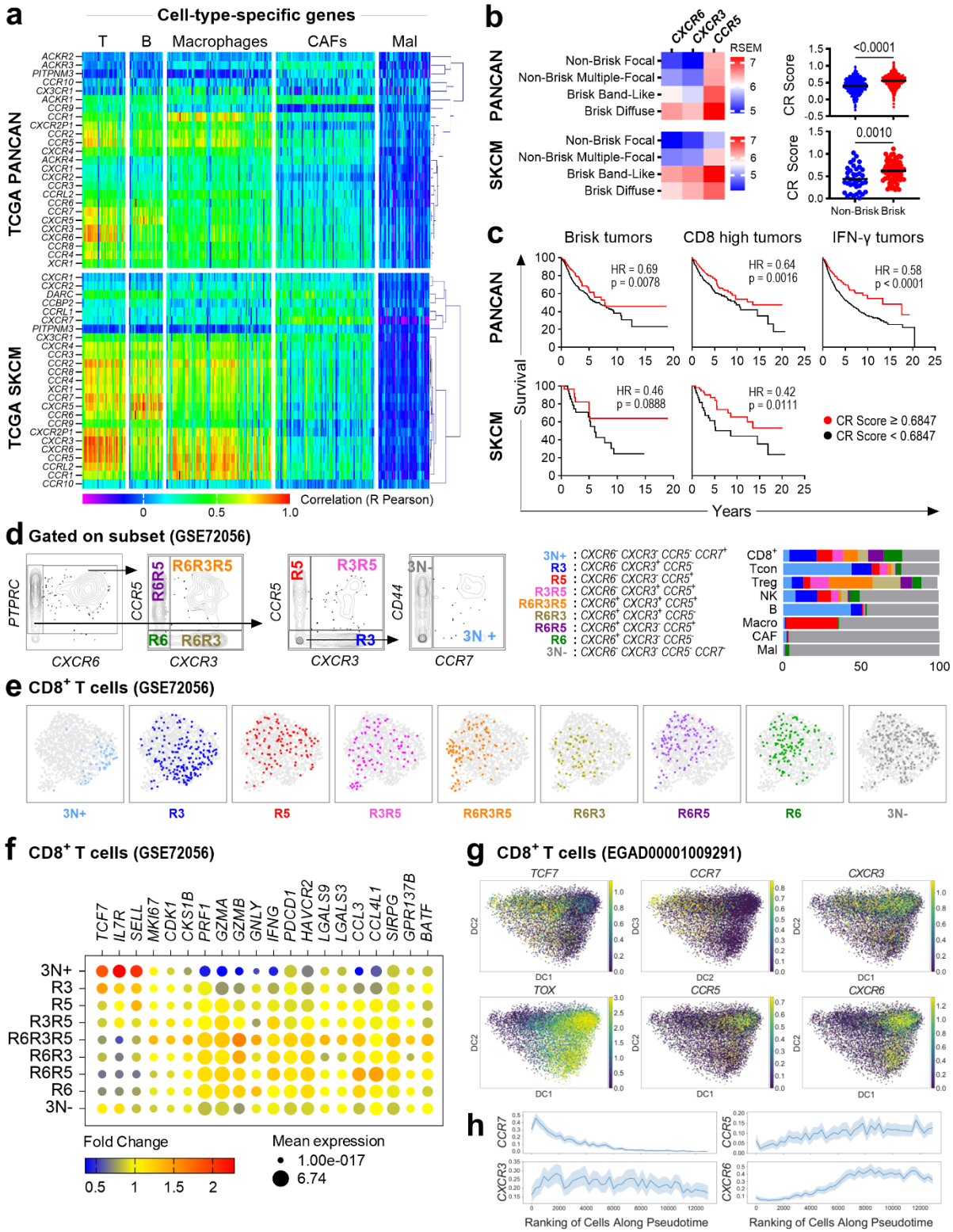
a
Cell-type-specific genes
T
B
Macrophages
CAFs
Mal
TCGA PANCAN
TCGA SKCM
Correlation (R Pearson)
b
CXCR6
CXCR3
CCR5
RSEM
PANCAN
SKCM
Non-Brisk Focal
Non-Brisk Multiple-Focal
Brisk Band-Like
Brisk Diffuse
CR Score
<0.0001
0.0010
Non-Brisk
Brisk
c
Brisk tumors
CD8 high tumors
IFN-γ tumors
HR = 0.69
p = 0.0078
HR = 0.64
p = 0.0016
HR = 0.58
p < 0.0001
HR = 0.46
p = 0.0888
HR = 0.42
p = 0.0111
Survival
Years
CR Score ≥ 0.6847
CR Score < 0.6847
d Gated on subset (GSE72056)
PTPRC
CXCR6
CCR5
CXCR3
CD44
CCR7
R6R5
R6R3R5
R6
R6R3
R5
R3R5
R3
3N-
3N+
3N+ : CXCR6- CXCR3- CCR5- CCR7+
R3 : CXCR6- CXCR3+ CCR5-
R5 : CXCR6- CXCR3- CCR5+
R3R5 : CXCR6- CXCR3+ CCR5+
R6R3R5 : CXCR6+ CXCR3+ CCR5+
R6R3 : CXCR6+ CXCR3+ CCR5-
R6R5 : CXCR6+ CXCR3- CCR5+
R6 : CXCR6+ CXCR3- CCR5-
3N- : CXCR6- CXCR3- CCR5- CCR7-
CD8+
Tcon
Treg
NK
B
Macro
CAF
Mal
e CD8+ T cells (GSE72056)
3N+
R3
R5
R3R5
R6R3R5
R6R3
R6R5
R6
3N-
f CD8+ T cells (GSE72056)
TCF7
IL7R
SELL
MKI67
CDK1
CKS1B
PRF1
GZMA
GZMB
GNLY
IFNG
PDCD1
HAVCR2
LGALS9
LGALS3
CCL3
CCL4L1
SIRPG
GPR137B
BATF
Fold Change
Mean expression
1.00e-017
6.74
g CD8+ T cells (EGAD00001009291)
TCF7
CCR7
CXCR3
TOX
CCR5
CXCR6
DC1
DC2
DC3
h
Ranking of Cells Along Pseudotime

322

**Figure 1. The landscape of chemokine receptor (CR) gene expression in human cancer reveals clustered T-cell expression of CXCR3, CCR5 and CXCR6 which define functional subsets and have prognostic importance. a and b.** *In-silico* analysis of tumor transcriptome from Pan-Cancer Atlas samples (TCGA-PANCAN; n=11323) and melanoma patients (TCGA-SKCM; n=475). **a.** Hierarchical-Cluster heatmap reveals correlation of CR gene expression with different cell types in all tumors (top) or melanoma (bottom) tumor microenvironment. Cells are defined by sets of cell-type-specific genes (Supplementary Table 1). **b.** Heatmaps show the expression of *CXCR6*, *CXCR3* and *CCR5* in TCGA-PANCAN and melanoma samples based on their "brisk" classification [33]. Dot plot reveals higher CR score (based on CXCR6, CXCR3 and CCR5 expression) on brisk versus non-brisk samples from PANCAN or melanoma patients. **c.** Kaplan-Meier survival curves categorized by CR score in TCGA (PANCAN or SKCM) samples confirm their prognostic potential in only brisk, $CD8^+$ high [34] or IFN-γ tumors [35]. **d to f**. *In-silico* analysis of single-cell transcriptome from metastatic melanoma (GSE72056). **d.** Gating strategy used to define cell subsets based on the co-expression of *CXCR6*, *CXCR3*, *CCR5*, and *CCR7* genes. Bar plot showing the higher heterogeneity of CR subsets in T cells in comparison to other populations in the metastatic melanoma microenvironment. **e**. UMAP multidimensional analysis showing CR-defined subsets with different genetic profiles in CD8+ T-cells. **f**. Dot plot gene expression of markers of naïve, cytotoxicity, exhaustion, transcription factors and cytokines reveal transcriptional differences of CR-positive subsets in CD8+ T-cells. **g and h**. *In-silico* analysis of single-cell transcriptome from metastatic melanoma (EGAD00001009291). Diffusion mapping and pseudotime inference analysis reveal differential enrichment (**g**) and pseudotemporal expression patterns (**h**) of *CCR7*, *CXCR3*, *CCR5* and *CXCR6* during *TCF7* to *TOX* $CD8^+$ T cell trajectory. <u>CR-defined subsets</u>: 3N+ (*CXCR6*$^-$, *CXCR3*$^-$, *CCR5*$^-$, *CCR7*$^+$), R3 (*CXCR6*$^-$, *CXCR3*$^+$, *CCR5*$^-$), R3R5 (*CXCR6-*, *CXCR3*$^+$, *CCR5*$^+$), R5 (*CXCR6*$^-$, *CXCR3*$^-$, *CCR5*$^+$), R6R3R5 (*CXCR6*$^+$, *CXCR3*$^+$, *CCR5*$^+$), R6R5 (*CXCR6*$^+$, *CXCR3*$^-$, *CCR5*$^+$), R6R3 (*CXCR6*$^+$, *CXCR3*$^+$, *CCR5*$^-$), R6 (*CXCR6*$^+$, *CXCR3*$^-$, *CCR5*$^-$) and 3N- (*CXCR6*$^-$, *CXCR3*$^-$, *CCR5*$^-$, *CCR7*$^-$).

**Extended Data Fig. 1.**

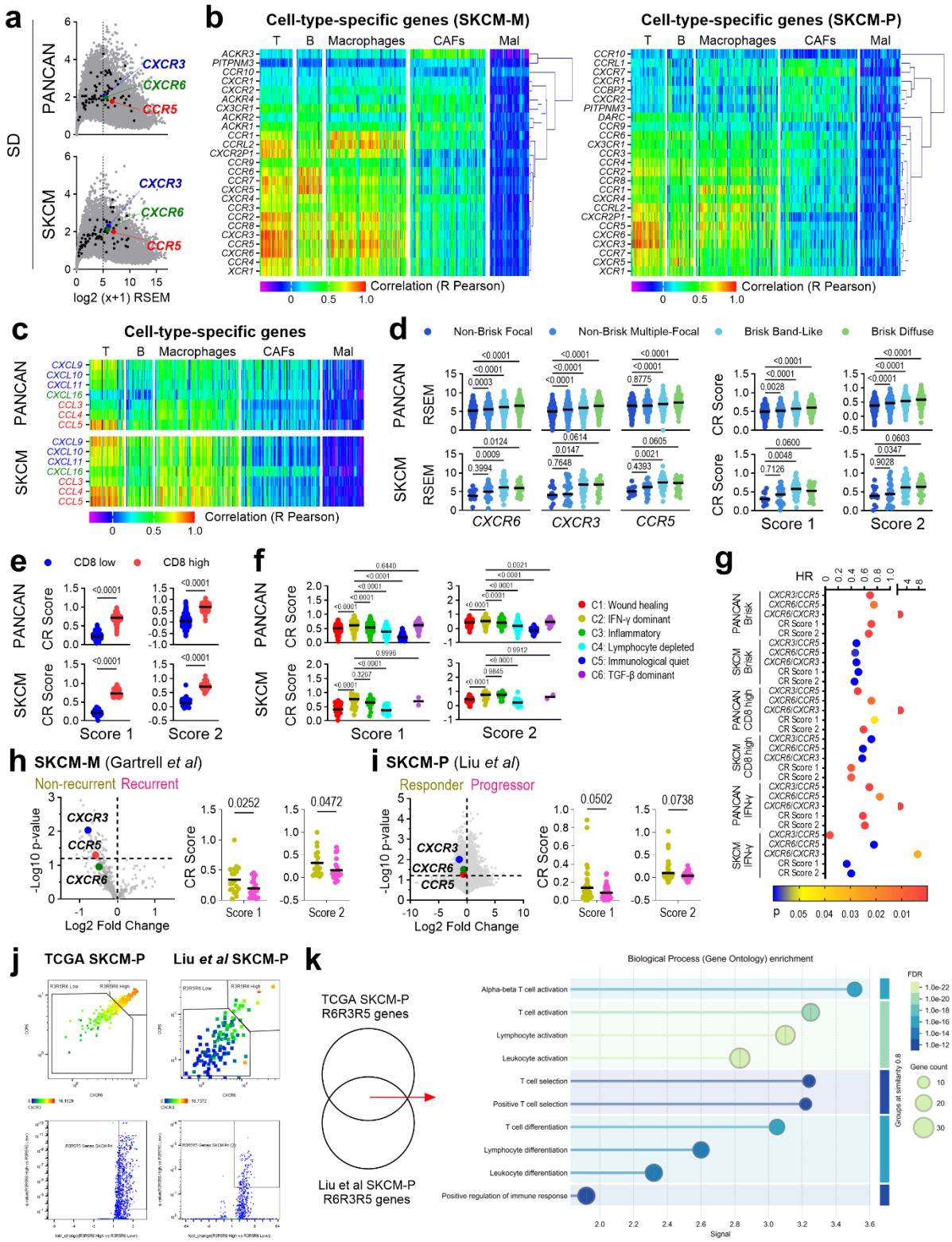

**Extended Data Fig. 1. a to c. Gene expression of chemokine receptors and their ligands in human cancer by sample type.** *In-silico* analysis of tumor transcriptome from Pan-Cancer Atlas samples (TCGA-PANCAN; n=11323) and melanoma patients (TCGA-SKCM; n=475). **a.** Mean-Variance Plot graph showing high expression of *CXCR3*, *CCR5* and *CXCR6* genes in PANCAN, or melanoma. Black dots represent genes for other chemokine receptors and chemokines. **b.** Hierarchical-Cluster heatmap reveals correlation of chemokine receptor gene expression with different tumor microenvironment cell-type-specific genes in metastatic and primary melanoma. **c**. Hierarchical-Cluster heatmap reveals correlation of CXCR3, CCR5 and CXCR6 ligands gene expression with different cell types in the tumor microenvironment in PANCAN and melanoma samples. Cell types were defined by cell-type-specific genes. **d.** Dot plots show the expression of *CXCR6*, *CXCR3, CCR5,* and CR scores (based on CXCR6, CXCR3 and CCR5 expression) in TCGA-PANCAN and melanoma samples based on their "brisk" classification [33]. **e and f**. Dot plots show the expression of CR scores (based on CXCR6, CXCR3 and CCR5 expression) in TCGA-PANCAN and melanoma samples based on their "$CD8^+$ score" [34] (**e**) or immune subtype [35] (**f**) classification. **g**. Dot plot represents the Hazard ratio (HR) and "p" value of CR scores and CR ratios (*CXCR3*/*CCR5*, *CXCR6*/*CCR5*, *CXCR6*/*CXCR3*) for survival prediction in only brisk, CD8 high or IFN-γ tumor from PANCAN or melanoma samples. **h and i**. Analysis of transcriptional data from human melanoma reveals higher CR scores in non-recurrent vs recurrent metastatic tumors [36] (**h**) and responders vs progressors primary tumors [37] (**i**). **j**. Identification of upregulated differentially expressed genes (DEGs) from TCGA and Liu *et al* primary melanoma samples with higher expression of *CXCR6*, *CXCR3*, and *CCR5* using SeqGeq. **j**. Dot plot graph showing the gene ontology analysis using shared upregulated DEGs from TCGA and Liu *et al* samples.

**Extended Data Fig. 2.**

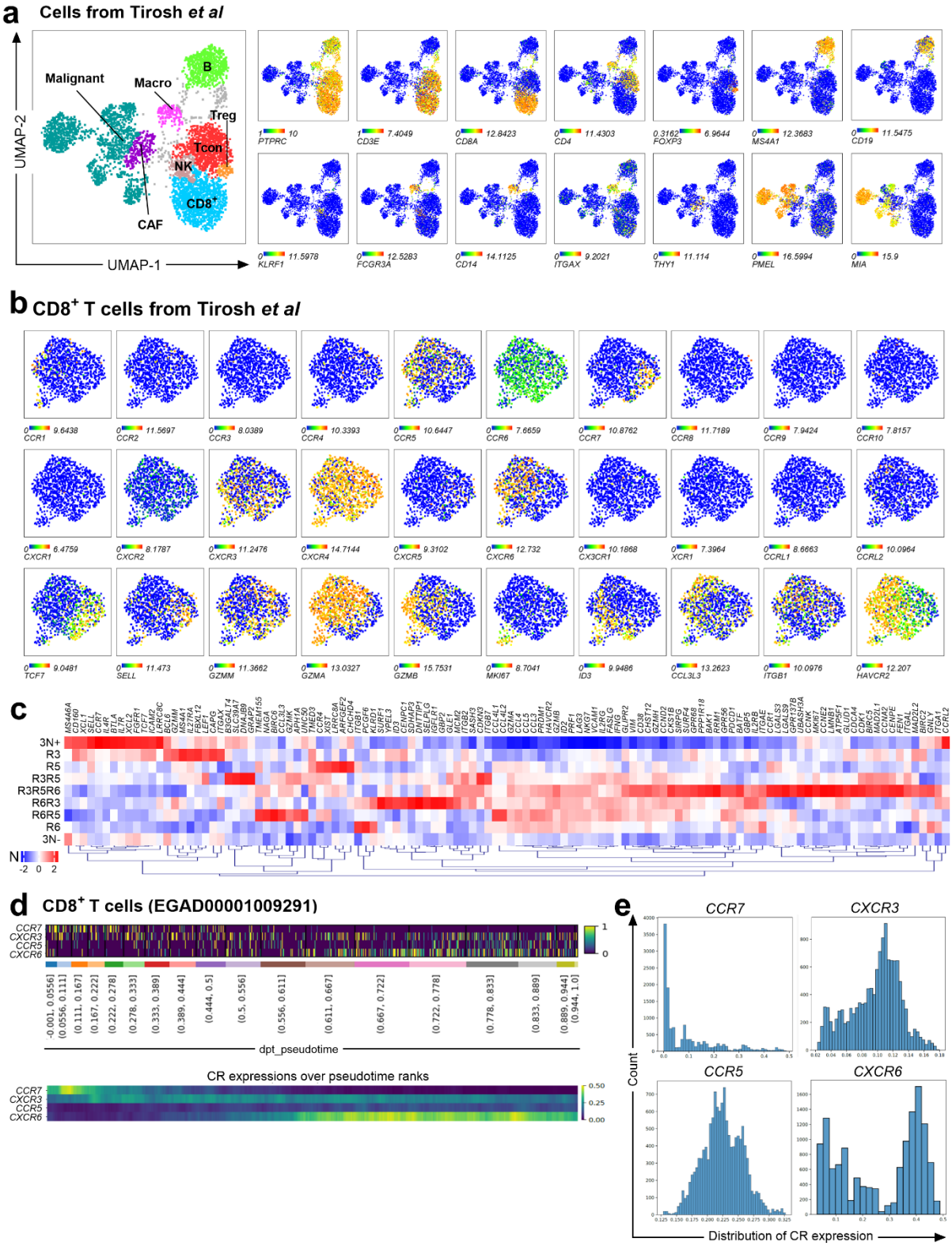


375

**Extended Data Fig. 2. a to c. Single-cell Gene expression of chemokine receptors at a single cell level in human metastatic melanoma** (GSE72056). **a.** UMAP multidimensional analysis identifies different immune populations based on immune gene expression in the tumor. **b.** UMAP multidimensional analysis of gene expression of naïve, cytotoxicity, exhaustion markers, transcription factors and chemokine receptors observed in $CD8^+$ T cells. **c**. Hierarchical-Clustering heatmap of gene expression of markers of naïve, cytotoxicity, exhaustion, transcription factors and cytokines reveal transcriptional differences of CR-positive subsets in CD8+ T-cells. **d and e. Trajectory of chemokine receptors in Melanoma.** *In-silico* single-cell gene expression analysis of human metastatic melanoma (EGAD00001009291). **d**. Rank sort and sliding window 300 cells of *CCR7*, *CXCR3*, *CCR5* and *CXCR6* gene expression across $CD8^+$ T cell trajectory inferred by diffusion pseudotime [46]. Pseudotime intervals are shown as colored bars. **e.** Distributions of normalized chemokine receptor (CR) expressions among $CD8^+$ T cell samples.

**Figure 2.**

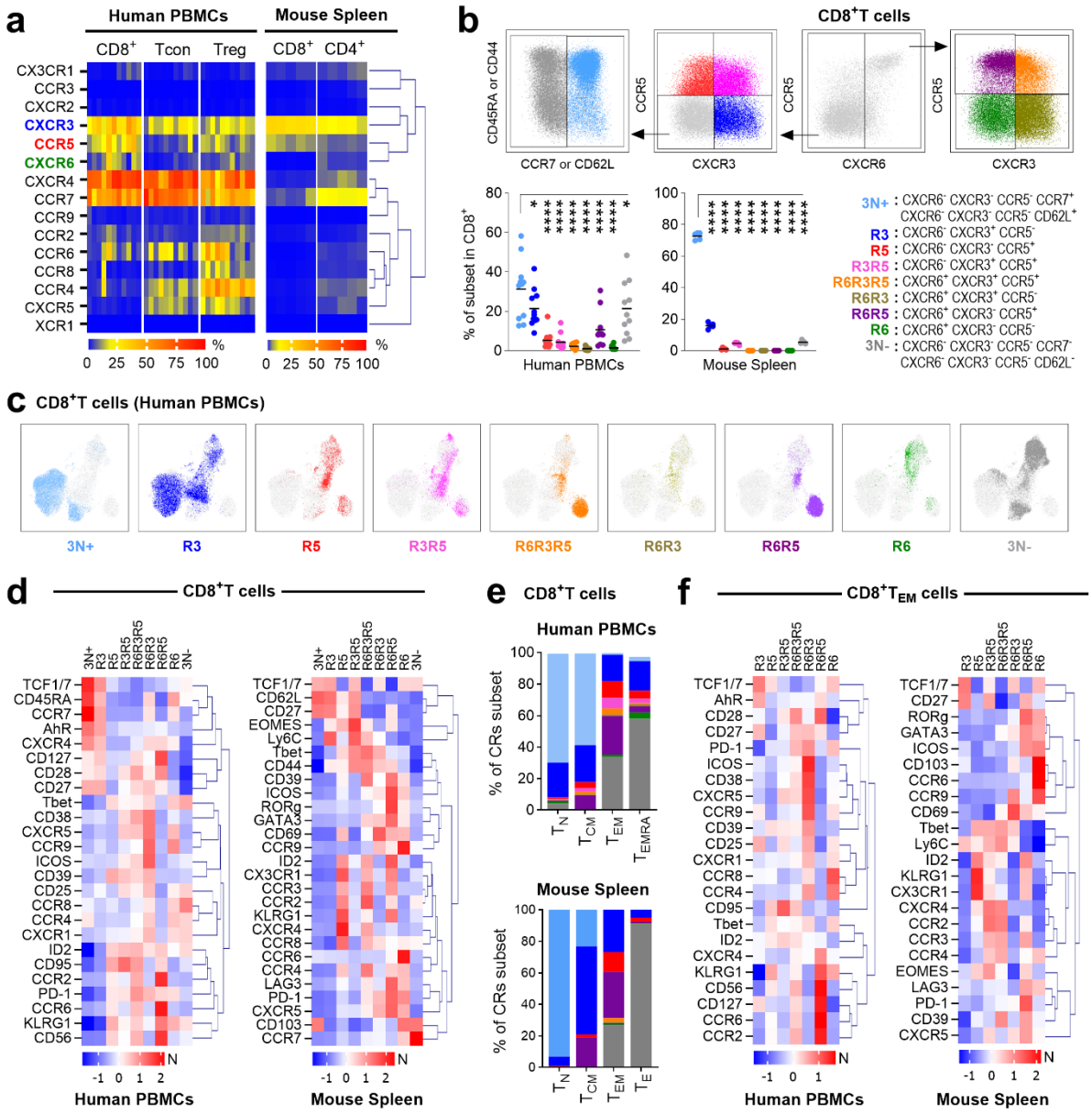


**Figure 2. Co-expression of CXCR3, CCR5 and CXCR6 proteins in human PBMCs and murine splenocytes reveals subsets with distinct differentiation profiles.** PBMCs from healthy human donors (n=11) and splenocytes from healthy C57BL/6J mice (n=5) were analyzed using flow cytometry. **a.** Hierarchical-Cluster heatmap analysis of T-cell subsets from human and mouse reveals co-expression of CXCR3, CCR5, CXCR6 and other chemokine receptors (CRs) in healthy conditions. **b.** Gating strategy used to identify CR subsets based on the surface co-expression of CXCR6, CXCR3, CCR5, and CCR7 (human) or CD62L (mouse). The percentages of T-cell subsets defined and color-coded by CR expression are represented in scatter dot plots in human and mouse. **c**. UMAP multidimensional analysis showing CR-defined subsets with different protein profiles in human CD8$^+$ T cells. **d**. Hierarchical-Cluster heatmap of normalized (N) protein

401 expression of CRs, transcription factors, activation and exhaustion markers reveal phenotypic
402 differences of CR-defined subsets in human and mouse $CD8^+$ T cells. **e**. Bar graphs showing the
403 distribution of CR-defined subsets within T-cell memory subsets reveal that T-effector memory
404 ($T_{EM}$) cells can be subdivided based on their co-expression of CRs in both human and mice. **f**.
405 Hierarchical-Cluster heatmap of normalized (N) protein expression of CRs, transcription factors,
406 activation and exhaustion markers also reveal phenotypic differences of CR-defined subsets in
407 human and murine $CD8^+$ $T_{EM}$ populations. The significance was calculated using unpaired Mann-
408 Whitney tests, *P < 0.05, **P < 0.01, ***P < 0.001, ****P < 0.0001. CR-defined subsets: 3N+
409 ($CXCR6^-$, $CXCR3^-$, $CCR5^-$, $CCR7^+$), R3 ($CXCR6^-$, $CXCR3^+$, $CCR5^-$), R3R5 ($CXCR6^-$, CXCR3+, $CCR5^+$), R5
410 ($CXCR6^-$, $CXCR3^-$, $CCR5^+$), R6R3R5 ($CXCR6^+$, $CXCR3^+$, $CCR5^+$), R6R5 ($CXCR6^+$, $CXCR3^-$, $CCR5^+$), R6R3
411 ($CXCR6^+$, $CXCR3^+$, $CCR5^-$), R6 ($CXCR6^+$, $CXCR3^-$, $CCR5^-$) and 3N- ($CXCR6^-$, $CXCR3^-$, $CCR5^-$, $CCR7^-$).

412 **Extended Data Fig. 3.**

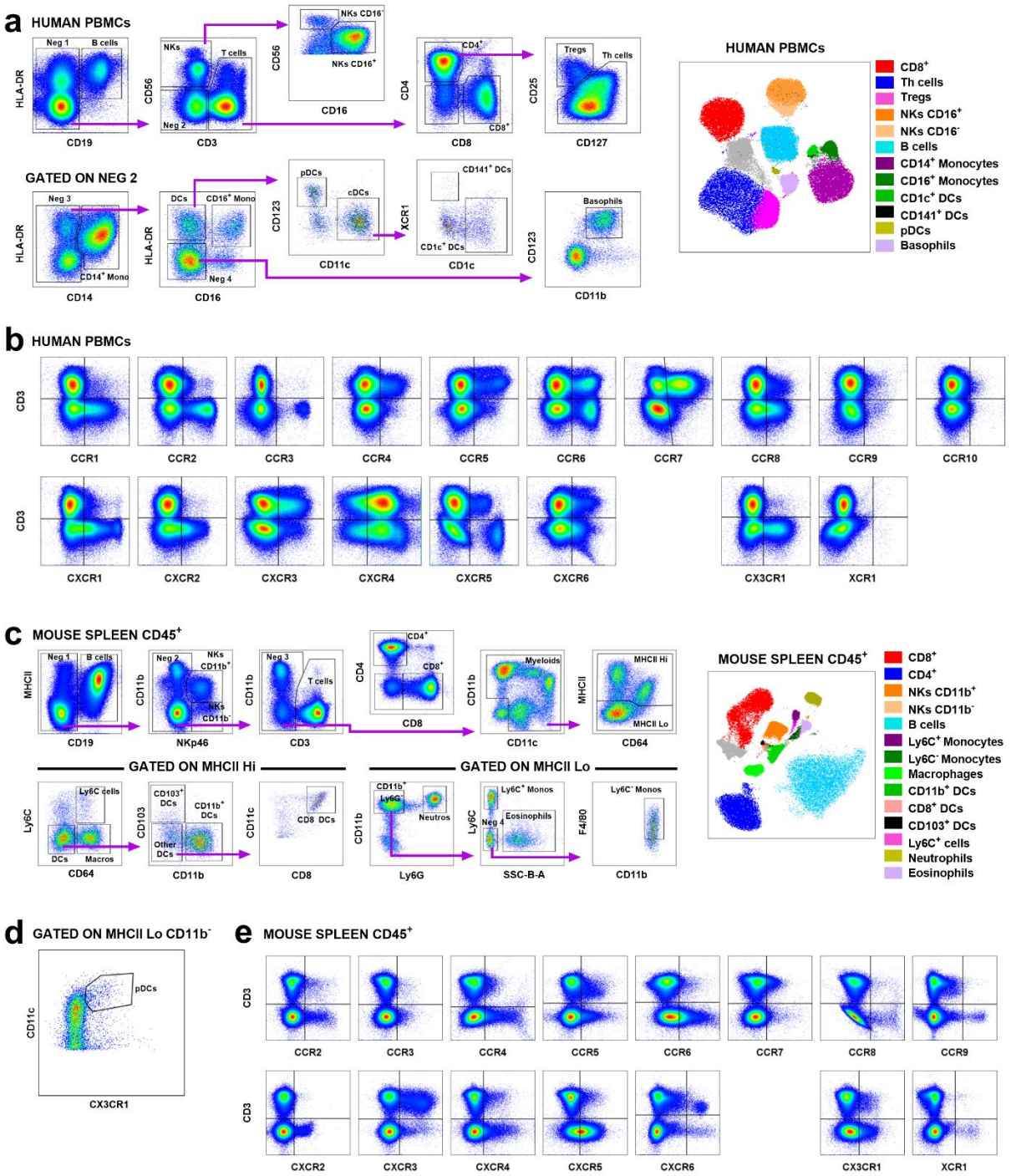


413

414 **Extended Data Fig. 3. Gating strategy used for multiparametric full spectral flow cytometry.**
415 PBMCs from healthy human donors (n=11) and splenocytes from healthy C57BL/6J female mice
416 (n=5) were analyzed using spectral flow cytometry. For human cells, we used multiparametric
417 spectral flow cytometry with a 43-color extracellular panel and 42-color intracellular panel and
418 for murine cells we used a 36-color extracellular panel and a 35-color intracellular panel to study

multiple leukocyte populations, chemokine receptor (CRs), and other markers. **a.** Classic gating strategy and UMAP multidimensional visualization used to identify human immune subsets. **b.** Representative plots showing CR expression in human PBMCs. **c, d.** Classic and multidimensional gating strategy used to identify murine immune subsets. **e.** Representative plots showing CR expression in murine splenocytes.

**Extended Data Fig. 4.**

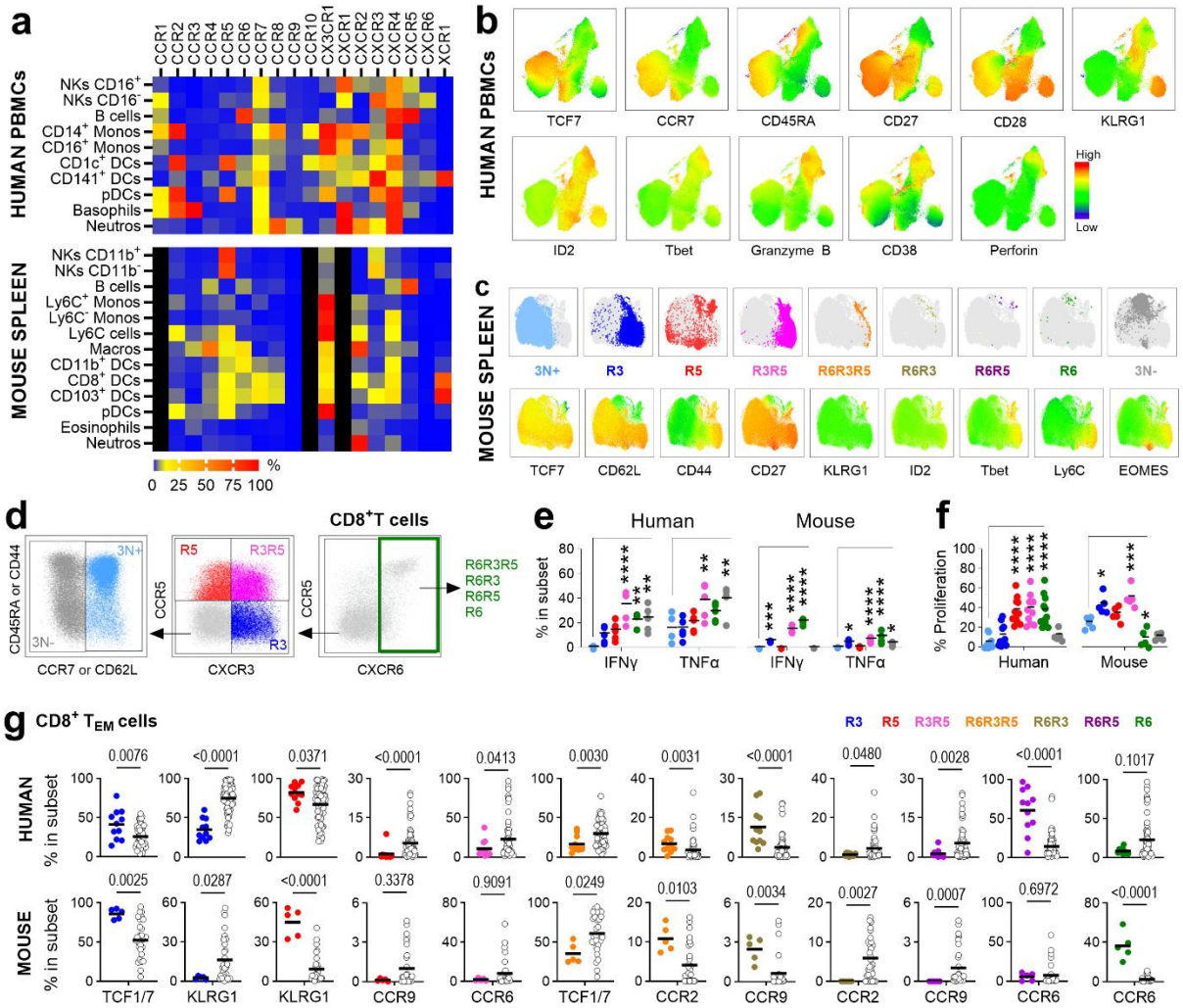


**Extended Data Fig. 4. Co-expression of CXCR3, CCR5 and CXCR6 proteins in human PBMCs and murine splenocytes reveals subsets with distinct function and differentiation profiles.** PBMCs from healthy human donors (n=11) and splenocytes from healthy C57BL/6J female mice (n=5) were analyzed using spectral flow cytometry. **a**. Heatmap analysis of immune subsets from humans and mice reveals the heterogeneity of expression and co-expression of chemokine receptors (CRs). **b**. UMAP multidimensional analysis showing protein expression of naïve, memory, activation and exhaustion markers in human CD8$^+$ T cells. **c**. UMAP multidimensional analysis showing CR-defined subsets with different naïve, memory, activation and exhaustion markers profiles in CD8$^+$ T-cells. **d to f**. CR-defined subsets were sorted from human PBMCs and murine splenocytes and stimulated for 2h to study activation and 2d for proliferation. **d**. Gating strategy to define CR subsets, green color refers to R6R3R5, R6R5, R6R3, and R6 subsets. Plots show that CR-defined subsets in CD8$^+$ T cells have different activation (**e**) and proliferation (**f**) profiles. **g**. Scatter dot plot of CD8$^+$ $T_{EM}$ cells showing the expression of proteins that are differentially expressed between a specific CR subset and the rest of subsets (white dots). Blacked out cells in heatmap represent blank values. The significance was calculated using unpaired

ANOVA or Mann-Whitney multiple comparisons tests, *P < 0.05, **P < 0.01, ***P < 0.001, ****P < 0.0001. CR-defined subsets: 3N+ (CXCR6$^-$, CXCR3$^-$, CCR5$^-$, CCR7$^+$), R3 (CXCR6$^-$, CXCR3$^+$, CCR5$^-$), R3R5 (CXCR6$^-$, CXCR3+, CCR5$^+$), R5 (CXCR6$^-$, CXCR3$^-$, CCR5$^+$), R6R3R5 (CXCR6$^+$, CXCR3$^+$, CCR5$^+$), R6R5 (CXCR6$^+$, CXCR3$^-$, CCR5$^+$), R6R3 (CXCR6$^+$, CXCR3$^+$, CCR5$^-$), R6 (CXCR6$^+$, CXCR3$^-$, CCR5$^-$) and 3N- (CXCR6$^-$, CXCR3$^-$, CCR5$^-$, CCR7$^-$).

447 **Figure 3.**

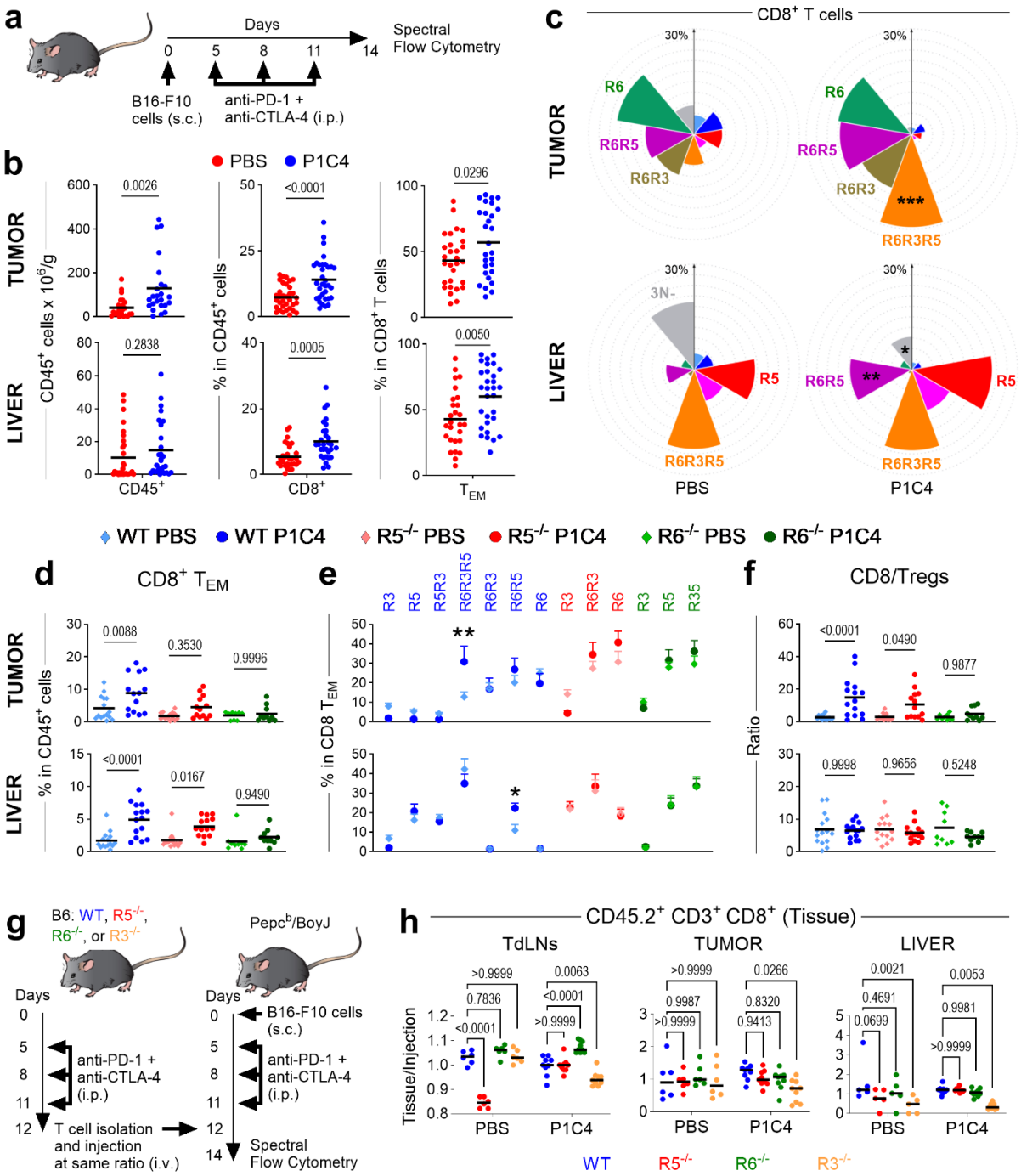


448

449 **Figure 3. Triple expression of CXCR3, CCR5 and CXCR6 is required for PD-1/CTLA4-induced**
450 **effector T-cell increase in melanoma tumors. a**. B16 tumor-bearing C57BL/6J female mice (n=15)
451 were treated with PD-1/CTLA-4 mAb on days 5, 8 and 11 (P1C4). Cells from tumors and liver were
452 isolated on day 14 and analyzed using spectral flow cytometry. **b.** P1C4 treatment increases the
453 numbers of tumor-infiltrating $CD45^+$ cells with no effect on liver, whereas levels of $CD8^+$ T or $T_{EM}$
454 cells in tumor and liver are increased after treatment. **c**. Nightingale Rose's charts show changes

455 of chemokine receptor (CR)-defined subsets after P1C4 treatment in tumor and liver in
456 comparison to the control group (* to *** representing significant differences between P1C4 and
457 PBS). **d to f**. B16 tumor-bearing C57BL/6J female wild-type (WT), CCR5$^{-/-}$ (R5$^{-/-}$) or CXCR6$^{-/-}$ (R6$^{-/-}$)
458 mice (n=10) were treated with P1C4 as described above. **d top**. P1C4 increase of CD8$^{+}$ $T_{EM}$
459 infiltration in the tumor was lost in either CCR5 or CXCR6 lacking mice. **d bottom**. P1C4-induced
460 increase of CD8$^{+}$ $T_{EM}$ infiltration in the liver was eliminated in R6$^{-/-}$ but not in R5$^{-/-}$ mice. **e**. R6R3R5
461 and R6R5 subsets are increased in CD8$^{+}$ $T_{EM}$ cells in tumor and liver respectively, after P1C4
462 treatment. Mice lacking CCR5 or CXCR6 showed no significant change in their CR-defined subsets
463 after P1C4 treatment. **f.** P1C4 treatment increased CD8/Treg ratio in WT tumors; this effect is
464 reduced in R5$^{-/-}$ mice and lost in R6$^{-/-}$ mice. No changes are observed in the liver. **g.** Female mice
465 (n=3) with C57BL/6J background (WT, R5$^{-/-}$, R6$^{-/-}$ and CXCR3$^{-/-}$ (R3$^{-/-}$)) were treated with P1C4 on
466 days 5, 8 and 11. T cells from spleen were isolated on day 12, labelled with CellTrace (excluding
467 GFP$^{+}$ R6$^{-/-}$), and injected at the same proportion into the tail of B16 tumor-bearing (Day 12)
468 PepBoy female mice (n=6) treated with P1C4 with the same regimen and the same groups (PBS
469 in PBS, P1C4 in P1C4). Mice were sacrificed after 48 hours and cells from tumors, liver, spleen
470 and tumor-draining lymph nodes (TdLNs) were isolated and analyzed using spectral flow
471 cytometry. **h**. CD45.2$^{+}$ CD3$^{+}$ (tissue: CD90.2$^{-}$) cells lacking CXCR3 showed reduced tissue/injection
472 ratio in P1C4-treated TdLNs, tumor and liver, while cells lacking CXCR6 are increased in TdLNs
473 from P1C4 mice. Significance was calculated using unpaired ANOVA or Mann-Whitney multiple
474 comparisons tests, *P < 0.05, **P < 0.01, ***P < 0.001, ****P < 0.0001. <u>CR-defined subsets</u>: 3N+
475 (CXCR6$^{-}$, CXCR3$^{-}$, CCR5$^{-}$, CCR7$^{+}$), R3 (CXCR6$^{-}$, CXCR3$^{+}$, CCR5$^{-}$), R3R5 (CXCR6$^{-}$, CXCR3+, CCR5$^{+}$), R5
476 (CXCR6$^{-}$, CXCR3$^{-}$, CCR5$^{+}$), R6R3R5 (CXCR6$^{+}$, CXCR3$^{+}$, CCR5$^{+}$), R6R5 (CXCR6$^{+}$, CXCR3$^{-}$, CCR5$^{+}$), R6R3
477 (CXCR6$^{+}$, CXCR3$^{+}$, CCR5$^{-}$), R6 (CXCR6$^{+}$, CXCR3$^{-}$, CCR5$^{-}$) and 3N- (CXCR6$^{-}$, CXCR3$^{-}$, CCR5$^{-}$, CCR7$^{-}$).

**Extended Data Fig. 5.**

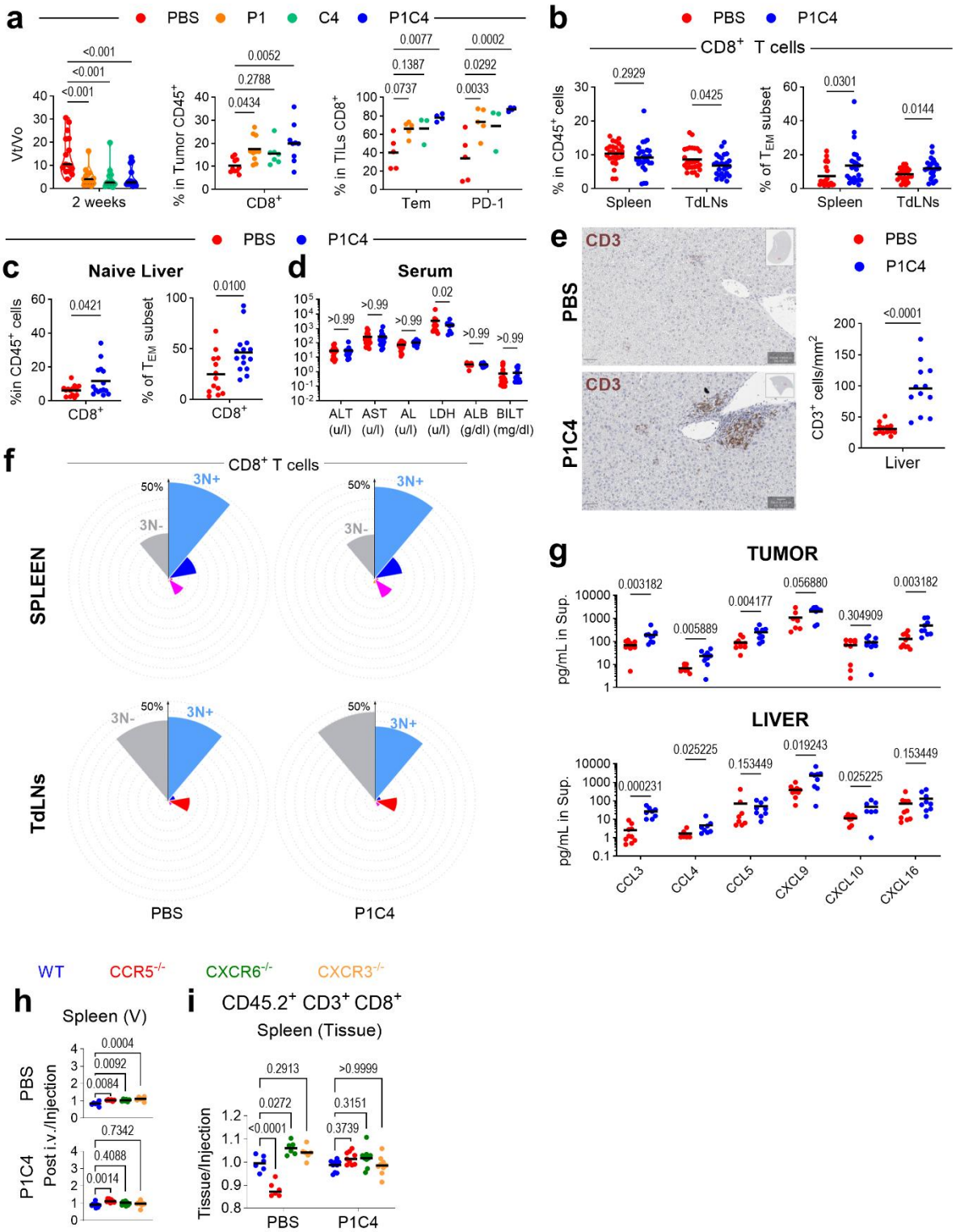

480 **Extended Data Fig. 5. Dual PD-1/CTLA4 blockade increases T-effector memory ($T_{EM}$) cells in B16**
481 **tumors and in target tissues of Immune-Related Adverse Events. a and b.** B16 tumor-bearing
482 C57BL/6J female mice (n=5-15) were treated with PD-1 (P1), CTLA-4 (C4) or both (P1C4) mAb on
483 days 5, 8 and 11. Cells from the spleen, tumor-draining lymph nodes (TdLNs), tumor and liver,
484 were isolated on day 14 and analyzed using spectral flow cytometry. **a**. Dual P1C4 blockade
485 showed the same tumor growth control at day 14 (**a left**, Vt = tumor volume at time t and Vo =
486 volume at baseline) but higher tumor infiltration of $CD8^+$ $T_{EM}$ in comparison with monotherapy
487 (**a center and right**). **b**. P1C4 treatment has no effect on levels of $CD8^+$ T cells in the spleen or
488 TdLNs but increases levels of $CD8^+$ $T_{EM}$ in these tissues. **c**. Livers from non-tumor bearing mice
489 show increased $CD8^+$ $T_{EM}$ levels after P1C4 treatment. **d**. Serum from mice treated with P1C4
490 reveals lower levels of lactate dehydrogenase (LDH) in comparison with control group, but other
491 serum markers such as alanine transaminase (ALT), aspartate transaminase (AST), alkaline
492 phosphatase (AL), albumin (ALB) and total bilirubin (BILT) were similar. **e**. Immunochemistry
493 staining of CD3 in the liver reveals increased levels of T cells in the tissue after P1C4 treatment in
494 comparison with PBS. **f**. Nightingale Rose's charts show no changes of chemokine receptor (CR)-
495 defined subsets after P1C4 treatment in spleen and TdLNs in comparison to the control group. **g**.
496 Scatter dot plots reveal an increase in the concentrations of CCR5, CXCR3 and CXCR6 ligands in
497 tumor and liver supernatant after P1C4 in comparison with controls. **h and i**. Female mice (n=3)
498 with C57BL/6J background (WT, $CCR5^{-/-}$, $CXCR6^{-/-}$ and $CXCR3^{-/-}$) were treated with P1C4 on days
499 5, 8 and 11 as described in Fig. 3i. **h**. A similar proportion of $CD8^+$ T cells from WT and genetic
500 knockout (KO) mice was confirmed before injection, with a vascular increase ($CD90.2^+$) of KO cells
501 after 48 hours. **i**. KO $CD8^+$ T cells have different percentages and tissue/injection ratio in the
502 spleen from recipient mice when compared to WT cells. Significance was calculated using
503 unpaired ANOVA or Mann-Whitney multiple comparisons tests. <u>CR-defined subsets</u>: 3N+ ($CXCR6^-$
504 , $CXCR3^-$, $CCR5^-$, $CCR7^+$), R3 ($CXCR6^-$, $CXCR3^+$, $CCR5^-$), R3R5 ($CXCR6^-$, CXCR3+, $CCR5^+$), R5 ($CXCR6^-$,
505 $CXCR3^-$, $CCR5^+$), R6R3R5 ($CXCR6^+$, $CXCR3^+$, $CCR5^+$), R6R5 ($CXCR6^+$, $CXCR3^-$, $CCR5^+$), R6R3 ($CXCR6^+$,
506 $CXCR3^+$, $CCR5^-$), R6 ($CXCR6^+$, $CXCR3^-$, $CCR5^-$) and 3N- ($CXCR6^-$, $CXCR3^-$, $CCR5^-$, $CCR7^-$).
507

508 **Figure 4.**

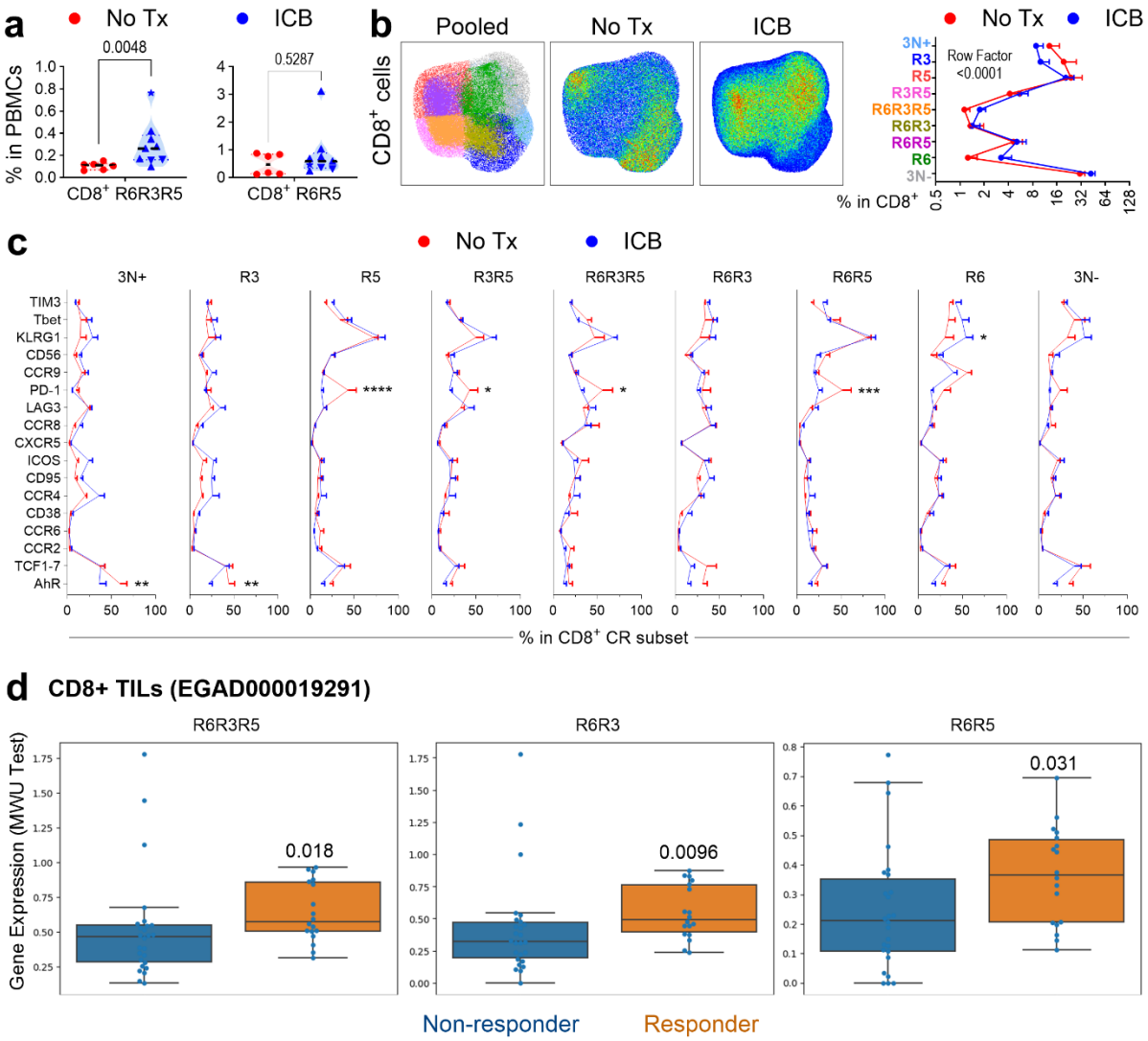


509

510 **Figure 4. PD-1/CTLA4 blockade changes CXCR6, CCR5 and CXCR3 co-expression in peripheral T**
511 **cells from melanoma patients.** PBMCs samples from melanoma patients (n=15) following
512 Immune Checkpoint Blockade (ICB, inverted triangles: early draw related to ICB, triangles: draw
513 in the middle of ICB, star: at the end of ICB) or not treatment (No Tx, circles) were analyzed using
514 full-spectral flow cytometry. **a**. Scatter dot plots showing that CD8$^+$ R6R3R5, and R6R5 subsets
515 are increased in the peripheral blood after P1C4. **b**. UMAP multidimensional analysis and
516 connecting dot plots reveal how ICB treatment changes CR subset profile of CD8$^+$ T cells. **c**.
517 Connecting dot plots showing molecular expression of chemokine receptors (CRs), transcription
518 factors, activation and exhaustion markers reveal phenotypic differences of CR-defined subsets
519 after treatment with ICB in CD8$^+$ T cells. **d**. Box plots showing gene expression (MWU Test) from
520 EGAD000019291 dataset reveal higher expression of R6R3R5, R6R3, and R6R5 signatures in ICB
521 responder patients in comparison to non-responders. The significance was calculated using
522 unpaired ANOVA or Mann-Whitney multiple comparisons tests, *P < 0.05, **P < 0.01, ***P <
523 0.001, ****P < 0.0001. CR-defined subsets: 3N+ (CXCR6$^-$, CXCR3$^-$, CCR5$^-$, CCR7$^+$), R3 (CXCR6$^-$,

524 CXCR3$^{+}$, CCR5$^{-}$), R3R5 (CXCR6$^{-}$, CXCR3$^{+}$, CCR5$^{+}$), R5 (CXCR6$^{-}$, CXCR3$^{-}$, CCR5$^{+}$), R6R3R5 (CXCR6$^{+}$,
525 CXCR3$^{+}$, CCR5$^{+}$), R6R5 (CXCR6$^{+}$, CXCR3$^{-}$, CCR5$^{+}$), R6R3 (CXCR6$^{+}$, CXCR3$^{+}$, CCR5$^{-}$), R6 (CXCR6$^{+}$,
526 CXCR3$^{-}$, CCR5$^{-}$) and 3N- (CXCR6$^{-}$, CXCR3$^{-}$, CCR5$^{-}$, CCR7$^{-}$).
527

528 **Extended Data Fig. 6.**

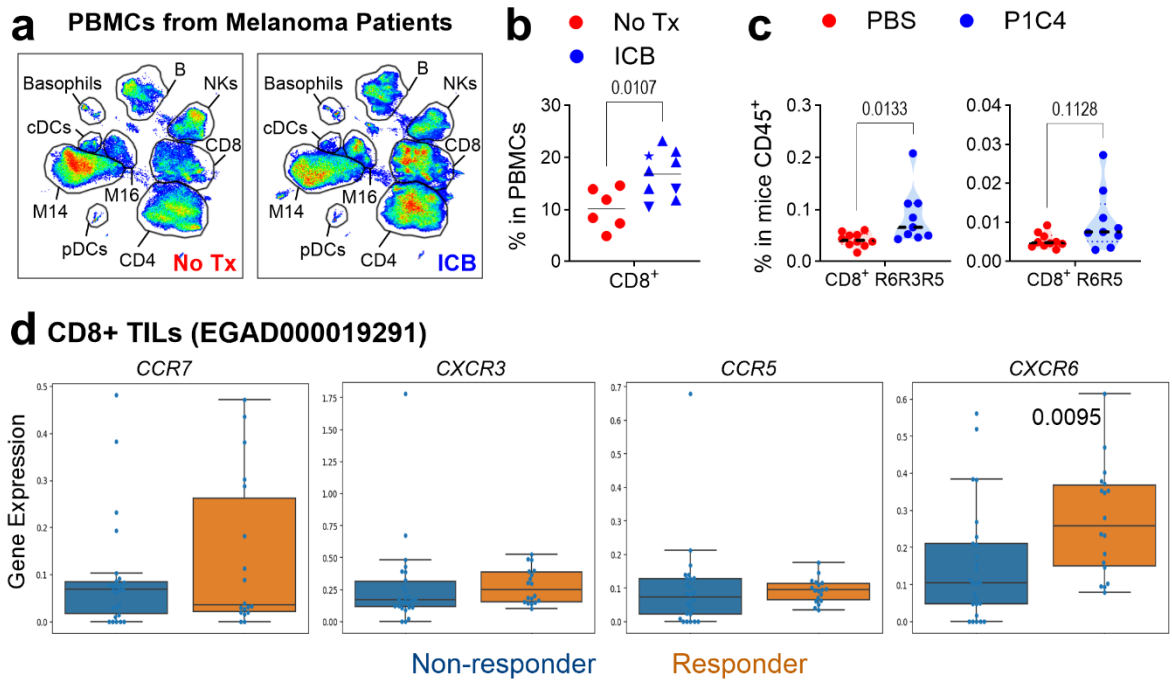


529

530 **Extended Data Fig. 6. PD-1/CTLA4 blockade changes CXCR6, CCR5 and CXCR3 co-expression in**
531 **peripheral T cells from melanoma patients. a and b.** PBMCs samples from melanoma patients
532 (n=15) following Immune Checkpoint Blockade (ICB, inverted triangles: early draw related to ICB,
533 triangles: draw in the middle of ICB, star: at the end of ICB) or not treatment (No Tx, circles) were
534 analyzed using full-spectral flow cytometry. ICB treatment significantly increases % of CD8 $T^+$ cells
535 as observed in the UMAP multidimensional analysis (**a**) and plot graphs (**b**). **c**. Scatter dot plots
536 show that $CD8^+$ R6R3R5 subsets are increased in the spleen of mice treated with P1C4 as
537 described in Fig. 3a. **d**. Box plots showing gene expression (MWU Test) from EGAD000019291
538 dataset reveals higher expression of *CXCR6* in ICB responder patients in comparison to non-
539 responders. The significance was calculated using unpaired ANOVA or Mann-Whitney multiple
540 comparisons tests. <u>CR-defined subsets</u>: 3N+ ($CXCR6^-$, $CXCR3^-$, $CCR5^-$, $CCR7^+$), R3 ($CXCR6^-$, $CXCR3^+$,
541 $CCR5^-$), R3R5 ($CXCR6^-$, $CXCR3^+$, $CCR5^+$), R5 ($CXCR6^-$, $CXCR3^-$, $CCR5^+$), R6R3R5 ($CXCR6^+$, $CXCR3^+$,
542 $CCR5^+$), R6R5 ($CXCR6^+$, $CXCR3^-$, $CCR5^+$), R6R3 ($CXCR6^+$, $CXCR3^+$, $CCR5^-$), R6 ($CXCR6^+$, $CXCR3^-$, $CCR5^-$
543 ) and 3N- ($CXCR6^-$, $CXCR3^-$, $CCR5^-$, $CCR7^-$).

544 **References**

545


546 1 Wolchok, J. D. *et al.* Final, 10-Year Outcomes with Nivolumab plus Ipilimumab in Advanced Melanoma. *N*
547 *Engl J Med* (2024). https://doi.org:10.1056/NEJMoa2407417
548 2 Morad, G., Helmink, B. A., Sharma, P. & Wargo, J. A. Hallmarks of response, resistance, and toxicity to
549 immune checkpoint blockade. *Cell* **184**, 5309-5337 (2021). https://doi.org:10.1016/j.cell.2021.09.020
550 3 Doki, Y. *et al.* Nivolumab Combination Therapy in Advanced Esophageal Squamous-Cell Carcinoma. *N Engl*
551 *J Med* **386**, 449-462 (2022). https://doi.org:10.1056/NEJMoa2111380
552 4 Wolchok, J. D. *et al.* Overall Survival with Combined Nivolumab and Ipilimumab in Advanced Melanoma. *N*
553 *Engl J Med* **377**, 1345-1356 (2017). https://doi.org:10.1056/NEJMoa1709684
554 5 Sznol, M. *et al.* Pooled Analysis Safety Profile of Nivolumab and Ipilimumab Combination Therapy in Patients
555 With Advanced Melanoma. *J Clin Oncol* **35**, 3815-3822 (2017). https://doi.org:10.1200/JCO.2016.72.1167
556 6 Motzer, R. J. *et al.* Nivolumab plus Ipilimumab versus Sunitinib in Advanced Renal-Cell Carcinoma. *N Engl J*
557 *Med* (2018). https://doi.org:10.1056/NEJMoa1712126
558 7 Sharma, P. *et al.* Nivolumab Plus Ipilimumab for Metastatic Castration-Resistant Prostate Cancer:
559 Preliminary Analysis of Patients in the CheckMate 650 Trial. *Cancer Cell* **38**, 489-499 e483 (2020).
560 https://doi.org:10.1016/j.ccell.2020.08.007
561 8 Hellmann, M. D. *et al.* Nivolumab plus Ipilimumab in Lung Cancer with a High Tumor Mutational Burden. *N*
562 *Engl J Med* **378**, 2093-2104 (2018). https://doi.org:10.1056/NEJMoa1801946
563 9 Overman, M. J. *et al.* Durable Clinical Benefit With Nivolumab Plus Ipilimumab in DNA Mismatch Repair-
564 Deficient/Microsatellite Instability-High Metastatic Colorectal Cancer. *J Clin Oncol*, JCO2017769901 (2018).
565 https://doi.org:10.1200/JCO.2017.76.9901
566 10 Gao, J. *et al.* Neoadjuvant PD-L1 plus CTLA-4 blockade in patients with cisplatin-ineligible operable high-risk
567 urothelial carcinoma. *Nat Med* **26**, 1845-1851 (2020). https://doi.org:10.1038/s41591-020-1086-y
568 11 Scherpereel, A. *et al.* Nivolumab or nivolumab plus ipilimumab in patients with relapsed malignant pleural
569 mesothelioma (IFCT-1501 MAPS2): a multicentre, open-label, randomised, non-comparative, phase 2 trial.
570 *Lancet Oncol* **20**, 239-253 (2019). https://doi.org:10.1016/S1470-2045(18)30765-4
571 12 Johncilla, M. *et al.* Ipilimumab-associated Hepatitis: Clinicopathologic Characterization in a Series of 11
572 Cases. *Am J Surg Pathol* **39**, 1075-1084 (2015). https://doi.org:10.1097/PAS.0000000000000453
573 13 Chen, P. L. *et al.* Analysis of Immune Signatures in Longitudinal Tumor Samples Yields Insight into
574 Biomarkers of Response and Mechanisms of Resistance to Immune Checkpoint Blockade. *Cancer Discov* **6**,
575 827-837 (2016). https://doi.org:10.1158/2159-8290.CD-15-1545
576 14 Daud, A. I. *et al.* Tumor immune profiling predicts response to anti-PD-1 therapy in human melanoma. *J Clin*
577 *Invest* **126**, 3447-3452 (2016). https://doi.org:10.1172/JCI87324
578 15 Rosenberg, S. A. *et al.* Durable complete responses in heavily pretreated patients with metastatic
579 melanoma using T-cell transfer immunotherapy. *Clin Cancer Res* **17**, 4550-4557 (2011).
580 https://doi.org:10.1158/1078-0432.CCR-11-0116
581 16 Rohaan, M. W. *et al.* Tumor-Infiltrating Lymphocyte Therapy or Ipilimumab in Advanced Melanoma. *N Engl*
582 *J Med* **387**, 2113-2125 (2022). https://doi.org:10.1056/NEJMoa2210233
583 17 Sarnaik, A. A. *et al.* Lifileucel, a Tumor-Infiltrating Lymphocyte Therapy, in Metastatic Melanoma. *J Clin*
584 *Oncol* **39**, 2656-2666 (2021). https://doi.org:10.1200/JCO.21.00612
585 18 Schulz, O., Hammerschmidt, S. I., Moschovakis, G. L. & Forster, R. Chemokines and Chemokine Receptors in
586 Lymphoid Tissue Dynamics. *Annu Rev Immunol* **34**, 203-242 (2016). https://doi.org:10.1146/annurev-
587 immunol-041015-055649
588 19 Bedognetti, D. *et al.* CXCR3/CCR5 pathways in metastatic melanoma patients treated with adoptive therapy
589 and interleukin-2. *Br J Cancer* **109**, 2412-2423 (2013). https://doi.org:10.1038/bjc.2013.557
590 20 Chheda, Z. S., Sharma, R. K., Jala, V. R., Luster, A. D. & Haribabu, B. Chemoattractant Receptors BLT1 and
591 CXCR3 Regulate Antitumor Immunity by Facilitating CD8+ T Cell Migration into Tumors. *J Immunol* **197**,
592 2016-2026 (2016). https://doi.org:10.4049/jimmunol.1502376
593 21 Hoch, T. *et al.* Multiplexed imaging mass cytometry of the chemokine milieus in melanoma characterizes
594 features of the response to immunotherapy. *Sci Immunol* **7**, eabk1692 (2022).
595 https://doi.org:10.1126/sciimmunol.abk1692

596 22 Bell, B., Flores-Lovon, K., Cueva-Chicana, L. A. & Macedo, R. Role of chemokine receptors in gastrointestinal
597 mucosa. *Int Rev Cell Mol Biol* **388**, 20-52 (2024). https://doi.org:10.1016/bs.ircmb.2024.02.003
598 23 Valdivia-Silva, J. & Chinney-Herrera, A. Chemokine receptors and their ligands in breast cancer: The key
599 roles in progression and metastasis. *Int Rev Cell Mol Biol* **388**, 124-161 (2024).
600 https://doi.org:10.1016/bs.ircmb.2024.07.002
601 24 Tang, Y., Hu, Y., Niu, Y., Sun, L. & Guo, L. CCL5 as a Prognostic Marker for Survival and an Indicator for
602 Immune Checkpoint Therapies in Small Cell Lung Cancer. *Front Med (Lausanne)* **9**, 834725 (2022).
603 https://doi.org:10.3389/fmed.2022.834725
604 25 Seitz, S. *et al.* CXCL9 inhibits tumour growth and drives anti-PD-L1 therapy in ovarian cancer. *Br J Cancer*
605 **126**, 1470-1480 (2022). https://doi.org:10.1038/s41416-022-01763-0
606 26 Han, Y. *et al.* CXCL10 and CCL5 as feasible biomarkers for immunotherapy of homologous recombination
607 deficient ovarian cancer. *Am J Cancer Res* **13**, 1904-1922 (2023).
608 27 Reschke, R. *et al.* Immune cell and tumor cell-derived CXCL10 is indicative of immunotherapy response in
609 metastatic melanoma. *J Immunother Cancer* **9** (2021). https://doi.org:10.1136/jitc-2021-003521
610 28 Fei, L., Ren, X., Yu, H. & Zhan, Y. Targeting the CCL2/CCR2 Axis in Cancer Immunotherapy: One Stone, Three
611 Birds? *Front Immunol* **12**, 771210 (2021). https://doi.org:10.3389/fimmu.2021.771210
612 29 Velasco-Velazquez, M. *et al.* CCR5 antagonist blocks metastasis of basal breast cancer cells. *Cancer research*
613 **72**, 3839-3850 (2012). https://doi.org:10.1158/0008-5472.CAN-11-3917
614 30 Sicoli, D. *et al.* CCR5 receptor antagonists block metastasis to bone of v-Src oncogene-transformed
615 metastatic prostate cancer cell lines. *Cancer research* **74**, 7103-7114 (2014). https://doi.org:10.1158/0008-
616 5472.CAN-14-0612
617 31 Halama, N. *et al.* Tumoral Immune Cell Exploitation in Colorectal Cancer Metastases Can Be Targeted
618 Effectively by Anti-CCR5 Therapy in Cancer Patients. *Cancer Cell* **29**, 587-601 (2016).
619 https://doi.org:10.1016/j.ccell.2016.03.005
620 32 Bachelerie, F. *et al.* International Union of Basic and Clinical Pharmacology. [corrected]. LXXXIX. Update on
621 the extended family of chemokine receptors and introducing a new nomenclature for atypical chemokine
622 receptors. *Pharmacol Rev* **66**, 1-79 (2014). https://doi.org:10.1124/pr.113.007724
623 33 Saltz, J., Gupta, R., Hou, L., Kurc, T., Singh, P., Nguyen, V., Samaras, D., Shroyer, K. R., Zhao, T., Batiste, R.,
624 Van Arnam, J., The Cancer Genome Atlas Research Network, Shmulevich, I., Rao, A. U. K., Lazar, A. J.,
625 Sharma, A., & Thorsson, V. Tumor-Infiltrating Lymphocytes Maps from TCGA H&E Whole Slide Pathology
626 Images [Data set]. (2018). https://doi.org:10.7937/K9/TCIA.2018.Y75F9W1
627 34 Wolf, D. Immune Signature Scores [Data set, https://pancanatlas.xenahubs.net]. (2016).
628 35 Thorsson, V. *et al.* The Immune Landscape of Cancer. *Immunity* **51**, 411-412 (2019).
629 https://doi.org:10.1016/j.immuni.2019.08.004
630 36 Gartrell, R. D. *et al.* Validation of Melanoma Immune Profile (MIP), a Prognostic Immune Gene Prediction
631 Score for Stage II-III Melanoma. *Clin Cancer Res* **25**, 2494-2502 (2019). https://doi.org:10.1158/1078-
632 0432.CCR-18-2847
633 37 Liu, D. *et al.* Integrative molecular and clinical modeling of clinical outcomes to PD1 blockade in patients
634 with metastatic melanoma. *Nat Med* **25**, 1916-1927 (2019). https://doi.org:10.1038/s41591-019-0654-5
635 38 Tirosh, I. *et al.* Dissecting the multicellular ecosystem of metastatic melanoma by single-cell RNA-seq.
636 *Science* **352**, 189-196 (2016). https://doi.org:10.1126/science.aad0501
637 39 Pozniak, J. *et al.* A TCF4-dependent gene regulatory network confers resistance to immunotherapy in
638 melanoma. *Cell* **187**, 166-183 e125 (2024). https://doi.org:10.1016/j.cell.2023.11.037
639 40 Saelens, W., Cannoodt, R., Todorov, H. & Saeys, Y. A comparison of single-cell trajectory inference methods.
640 *Nat Biotechnol* **37**, 547-554 (2019). https://doi.org:10.1038/s41587-019-0071-9
641 41 Yanagihara, T., Tanaka, K. & Matsumoto, K. A measuring method for occupancy of immune checkpoint
642 inhibitors in the cell surface. *Biochem Biophys Res Commun* **527**, 213-217 (2020).
643 https://doi.org:10.1016/j.bbrc.2020.04.122
644 42 Wong, M. T. *et al.* A High-Dimensional Atlas of Human T Cell Diversity Reveals Tissue-Specific Trafficking
645 and Cytokine Signatures. *Immunity* **45**, 442-456 (2016). https://doi.org:10.1016/j.immuni.2016.07.007
646 43 Berahovich, R. D., Lai, N. L., Wei, Z., Lanier, L. L. & Schall, T. J. Evidence for NK cell subsets based on
647 chemokine receptor expression. *J Immunol* **177**, 7833-7840 (2006).
648 https://doi.org:10.4049/jimmunol.177.11.7833

649 44 Franciszkiewicz, K., Boissonnas, A., Boutet, M., Combadiere, C. & Mami-Chouaib, F. Role of chemokines and
650 chemokine receptors in shaping the effector phase of the antitumor immune response. *Cancer Res* **72**,
651 6325-6332 (2012). https://doi.org:10.1158/0008-5472.CAN-12-2027
652 45 Ozga, A. J., Chow, M. T. & Luster, A. D. Chemokines and the immune response to cancer. *Immunity* **54**, 859-
653 874 (2021). https://doi.org:10.1016/j.immuni.2021.01.012
654 46 Haghverdi, L., Buettner, F. & Theis, F. J. Diffusion maps for high-dimensional single-cell analysis of
655 differentiation data. *Bioinformatics* **31**, 2989-2998 (2015). https://doi.org:10.1093/bioinformatics/btv325
656 47 Villablanca, E. J. & Mora, J. R. Competitive homing assays to study gut-tropic t cell migration. *J Vis Exp* (2011).
657 https://doi.org:10.3791/2619
658 48 Anderson, K. G. *et al.* Intravascular staining for discrimination of vascular and tissue leukocytes. *Nat Protoc*
659 **9**, 209-222 (2014). https://doi.org:10.1038/nprot.2014.005
660 49 Aran, D. *et al.* Reference-based analysis of lung single-cell sequencing reveals a transitional profibrotic
661 macrophage. *Nat Immunol* **20**, 163-172 (2019). https://doi.org:10.1038/s41590-018-0276-y
662 50 Lopez, R., Regier, J., Cole, M. B., Jordan, M. I. & Yosef, N. Deep generative modeling for single-cell
663 transcriptomics. *Nat Methods* **15**, 1053-1058 (2018). https://doi.org:10.1038/s41592-018-0229-2
664

## Methods

### Human samples

All study participants signed a written informed consent before inclusion in the study, and the protocols were approved by the Columbia University institutional review board (IRB). Peripheral blood mononuclear cells (PBMCs) were obtained from melanoma patients by Ficoll gradients and cryopreserved. PBMCs from healthy donors were obtained by Ficoll gradients and freshly analyzed using spectral flow cytometry. Characteristics of patients and healthy donors are summarized in Supplementary Table 4.

### Cell lines

B16-F10 cell line was a gift from Dr. Vonderheide. B16-F10 cells were cultured at 37°C in Dulbecco's Modified Eagle Media, supplemented with 10% FBS, 100 U $ml^{-1}$ penicillin and 100 µg $ml^{-1}$ streptomycin, 2 mM L-glutamine. All cell lines were determined to be free of Mycoplasma (Lonza) and common mouse pathogens (IDEXX).

### *In vivo* mouse studies

All mice were used according to approved protocols by Columbia University Institutional Animal Care and Use Committee (IACUC). Female mice, including C57BL/6J (B6) (Jax #000664), B6.129P2-*Ccr5*$^{tm1Kuz}$/J (Jax #005427), B6.129P2-*Cxcr6*$^{tm1Litt}$/J (Jax #005693), B6.129P2-*Cxcr3*$^{tm1Dgen}$/J (Jax #005796), and B6.SJL-*Ptprc*$^{a}$*Pepc*$^{b}$/BoyJ (Jax #002014) were obtained from The Jackson Laboratory at 7-12 weeks of age and were used for studies one week or more after their arrival in the animal barrier facility of the Columbia Center for Translational Immunology. For B16-F10 melanoma, $1 \times 10^5$ B16-F10 cells diluted in PBS were mixed with an equal volume of Matrigel (Corning) and subcutaneously injected in the right flank of B6 mice on day 0. Blocking antibodies were given on days 5, 8 and 11 after tumor implantation. Antibodies used for *in vivo* immune checkpoint blockade experiments were given intraperitoneally at a dose of 200 mg per mouse and included: CTLA4 (9H10) and PD-1 (RMP1-14) (BioXCell). Tumor diameters were measured using calipers. Volume was calculated using the formula: (length × width$^2$)/2. Mice were euthanized when tumor burden reached a volume of 1500 $mm^3$. Normalized tumor response to treatment is the measured volume at time t (Vt) relative to volume at baseline (Vo).

### Preparation of murine single-cell suspensions for flow cytometry

Murine cell suspensions were obtained from tumors or livers by a combination of GentleMACS (Miltenyi Biotec) dissociation and enzymatic dissociation using 1 mg/mL of collagenase IV (Sigma-Aldrich) and 0.2 mg/mL of DNase (Roche), followed by incubation with ACK Lysis buffer (Life Technologies) for 1 minute to remove red blood cells. For tumor-draining lymph nodes, mechanical and enzymatic dissociation was performed. After enzymatic incubation, samples were filtered through a 70-µm nylon cell strainer (Falcon). Splenocytes were obtained by dissociation using a 70-µm nylon cell strainer (Falcon) followed by ACK lysis buffer incubation for 1 minute. Cell suspensions were counted using Trypan Blue for cell viability.

### Flow cytometry and cell sorting

703 For flow cytometric analysis, live/dead cell discrimination was performed using Zombie NIR
704 Fixable Viability dye (Biolegend) or eFluor780 Fixable Viability Dye (eBiosciences). Fc receptors
705 were blocked using 2.4G2 anti-mouse CD16/CD32 (BD Pharmingen) or Human TruStain FcX
706 (Biolegend). Cell surface staining was done for 15 min at 36°C, followed by 15 min at 4°C.
707 Intracellular staining was done using a fixation/permeabilization kit (eBioscience). For human
708 cells, we used multiparametric spectral flow cytometry with a 43-color extracellular panel and
709 42-color intracellular panel that allowed us to study multiple leukocyte populations, CRs, and
710 functional markers simultaneously. In a similar way, for murine cells we used a 36-color
711 extracellular panel and a 35-color intracellular panel to study multiple leukocyte populations,
712 CRs, and other markers. For certain murine experiments traditional flow cytometry was used to
713 identify T cell populations. All flow cytometric analyses were performed using Aurora 5 lasers
714 (Cytek) or Fortessa II (BD) and analyzed using FlowJo software (BD). Cell sorting of CR-defined
715 subsets was performed using an Influx Cell Sorter (BD). Human and murine sorted cells were
716 stained with CellTrace kit followed by stimulation with Phorbol 12-myristate 13-acetate (PMA)
717 for 2 hours to study activation or 2 days for proliferation. See Supplementary Table 3 for a list of
718 antibodies used.

719 **Competitive homing experiment**

720 To determine the role of each individual CR in homing and tissue-infiltration of T cells, we
721 performed a competitive short-term homing strategy [47] to identify four groups of cells injected
722 at identical proportions. First, we treated WT, $CCR5^{-/-}$, $CXCR6^{-/-}$, or CXCR3 -/- mice with anti-PD-1
723 + anti-CTLA-4 (P1C4) or PBS on days 5, 8, and 11. On Day 12, mice were euthanized, and T cells
724 were isolated from the spleen using Pan T Cell Isolation Kit II (Miltenyi Biotec). After labelling T
725 cells with different CellTrace Kits (except $R6^{-/-}$ mice which express GFP reporter) and combining
726 them at similar proportion, $15 \times 10^6$ T cells were injected into the tail vein of B16 tumor-bearing
727 PepBoy mice (Day 12 after tumor injection), also treated with PBS or P1C4 following the same
728 treatment schedule and respecting the same group (PBS in PBS, P1C4 in P1C4). After 48 hours
729 recipient mice were intravenously injected with anti-CD90.2 antibody for discrimination between
730 vascular (circulating) and tissue lymphocytes [48]. After 3 minutes, mice were sacrificed, and the
731 percentage of WT, $CCR5^{-/-}$, $CXCR6^{-/-}$, or $CXCR3^{-/-}$ in $CD45.2^+$ $CD3^+$ cells in each tissue was divided
732 by the percentage of the same cells before injection.

733 **Immunohistochemistry of mouse tissues**

734 For liver immunohistochemistry, rabbit anti-CD3ε antibody (Invitrogen SP7) was diluted 1:100
735 and incubated at room temperature for 2 hours. Signal amplification was performed using
736 ImmPRESS Horse anti-rabbit IgG antibody-HRP (Vector) and DAB substrate Kit (BD Pharmingen)
737 following the manufacturer's protocol. Slides were counterstained and mounted.

738 **TCGA RNAseq**

739 RNAseq data was downloaded from the TCGA Pan-Cancer and TCGA Melanoma (SKCM) cohorts
740 from xenabrowser.net [51] (IDs: EB++AdjustPANCAN_IlluminaHiSeq_RNASeqV2.geneExp.xena and
741 TCGA.SKCM.sampleMap/HiSeqV2; unit: log2(norm_count + 1)), and corresponding phenotype
742 datasets (IDs: Survival_SupplementalTable_S1_20171025_xena_sp, survival/SKCM_survival.txt,

743 TCGA_phenotype_denseDataOnlyDownload.tsv, TCGA.SKCM.sampleMap/SKCM_clinicalMatrix).
744 This dataset contained 11060 samples for PANCAN and 464 samples for SKCM, but only primary
745 and metastatic tumors were analyzed (n=10272 for PANCAN, n=104 for primary SKCM, and n=368
746 for metastatic SKCM). R value from Pearson correlation between normalized RSEM counts (> 5
747 log2(x+1)) of CRs/ligands and cell-type-specific genes (Supplementary Table 1; based on Tirosh
748 et al) was calculated using GraphPad Prism v10. Then, an unsupervised hierarchical clustering
749 gene tree was generated based on these correlations using Multi Experiment Viewer (MeV) v4.9
750 [52]. For survival analysis, optimal cutoffs were calculated using Kaplan-Meier Plotter (kmplot.com)
751 [53], and Kaplan-Meier curves and Log-rank p values were generated using GraphPad Prism v10.
752 Identification of upregulated differentially expressed genes from TCGA and Liu *et al* primary
753 melanoma samples was done using SeqGeq (BD), a platform that allows visualization of scRNA
754 seq data and RNA seq data. STRING database (https://string-db.org/), was used to generate
755 biological process gene ontology analysis [54].

756 **Analysis of publicly available single-cell datasets**

757 To perform an *in-silico* analysis of single-cell RNA seq data from human metastatic melanoma,
758 the GSE72056_melanoma_single_cell_revised_v2.txt.gz file was downloaded from GEO Series
759 GSE72056. Using SeqGeq (BD), a characterization of immune and non-immune cells in the TME
760 was performed with UMAP multidimensional analysis. Subsets were defined in $CD8^+$ T cells by
761 the co-expression of *CCR7*, *CXCR6*, *CXCR3* and *CCR5* following the gating strategy defined in Fig.
762 1d left. Finally, gene expression of other functional markers was measured within CR-defined
763 subsets.

764 **scRNA-seq analysis of external clinical melanoma cohort immune cells**

765 Pre-processed scRNA-seq datasets of immune cells (n=49,009) from patients studied in Pozniak
766 et. al [39] were loaded into Seurat in R and subsequently Scanpy in Python. Immune cell annotation
767 was guided by automatic annotation using SingleR and its built-in reference dataset of stroma
768 and immune cells 'BlueprintEncodeData' as previously described [49]. Non-cycling $CD8^+$ T cell
769 subtypes (n=13,304) were selected for downstream analysis in Scanpy. The top 8,000 highly
770 variable genes were calculated using the 'Seurat_V3' method implemented in Scanpy. Gene
771 expression counts were normalized to median total counts and logarithmized in Scanpy. $CD8^+$ T
772 cells from individual samples were batch corrected using an scVI model trained with two hidden
773 layers and 30-dimensional latent space [50]. After performing neighborhood graph construction
774 using 20 nearest neighbors in scVI latent space, leiden clustering with default resolution, and
775 evaluation of known marker genes and $CD8^+$ T cell gene signatures in Scanpy, a noisy outlier
776 cluster was removed to prevent distortions in subsequent diffusion maps. Then, after
777 reconstructing the neighborhood graph using 300 nearest neighbors in scVI space, we computed
778 diffusion components (DCs) using the Scanpy implementation to examine continuous phenotypic
779 dynamics. The first and second DCs reflected expected *TCF7*$^+$ to *TOX*$^+$ progression of $CD8^+$ T cells,
780 and diffusion pseudotime along this trajectory was computed using the Scanpy implementation
781 to reflect this progression. We then plotted the expression of *CCR7*, *CXCR3*, *CCR5*, and *CXCR6*
782 across pseudotime using $CD8^+$ T cells ordered by diffusion pseudotime rank. Given the sparsity of
783 CR expression, which is typical for a clinical scRNA-seq dataset, we used sliding windows of 300
784 cells to average normalized expression across the $CD8^+$ T cell trajectory. We also computed the

785 95% confidence interval on the same window of 300 cells to reflect variation in expression across
786 the trajectory. The window size of 300 reduced sparsity while still conserving the expected
787 negative binomial distribution of CR gene expression counts. To compare CR expression patterns
788 over $CD8^+$ T cell trajectory, expression of each CR was scaled and plotted across cell pseudotime
789 rank, reflecting the expected progression of *CCR7*$^+$ to *CXCR6*$^+$ expression in $CD8^+$ T cells. Finally,
790 we examined differential expression of CR genes and the R6 co-expressing signatures (R6R3,
791 R6R5, R6R3R5) across ICB responder/non-responder clinical groups using average gene
792 expression pseudobulked by sample (summation of counts in each sample divided by total
793 number of cells in each sample) to account for CR expression sparsity and intrapatient
794 heterogeneity. Pseudobulked sample gene expression and signature expression were compared
795 across clinical groups using boxplots and significance was assessed using Mann-Whitney U-tests.
796 Code relating to this data analysis is publicly available on GitHub:
797 https://github.com/azizilab/chemokine_receptor_reproducibility.

798 **Statistical analysis**

799 One-way ANOVA was used for normally distributed data. Mann–Whitney was used for non-
800 parametric data. Kaplan–Meier log-rank analysis was used to evaluate the survival differences
801 between groups. Statistical analysis was conducted using Prism 10.0 software (GraphPad). Only
802 p values $< 0.05$ were considered as significant.

803 **Methods Bibliography.**

804 51. Goldman, M.J., Craft, B., Hastie, M. et al. Visualizing and interpreting cancer genomics data
805 via the Xena platform. Nat Biotechnol (2020). https://doi.org/10.1038/s41587-020-0546-8

806 52. Saeed AI, Sharov V, White J, Li J, Liang W, Bhagabati N, Braisted J, Klapa M, Currier T,
807 Thiagarajan M, Sturn A, Snuffin M, Rezantsev A, Popov D, Ryltsov A, Kostukovich E, Borisovsky I,
808 Liu Z, Vinsavich A, Trush V, Quackenbush J. TM4: a free, open-source system for microarray data
809 management and analysis. Biotechniques. 2003 Feb;34(2):374-8

810 53. Lanczky A, Gyorffy B. Web-Based Survival Analysis Tool Tailored for Medical Research
811 (KMplot): Development and Implementation, J Med Internet Res, 2021; 23(7):e27633,
812 doi:10.2196/27633

813 54. Szklarczyk D, Kirsch R, Koutrouli M, Nastou K, Mehryary F, Hachilif R, Gable AL, Fang T,
814 Doncheva NT, Pyysalo S, Bork P, Jensen LJ, von Mering C. The STRING database in 2023: protein-
815 protein association networks and functional enrichment analyses for any sequenced genome of
816 interest. Nucleic Acids Res. 2023 Jan 6;51(D1):D638-D646. doi: 10.1093/nar/gkac1000.